Title

Genetically Controlled Iron Oxide Biomineralization in Encapsulin Nanocompartments for Magnetic Manipulation of a Mammalian Cell Line

Authors

Efremova, Maria V

Wiedwald, Ulf

Sigmund, Felix

et al.

Publication Date

2025

DOI

10.1002/adfm.202418013

ADVANCED FUNCTIONAL MATERIALS
www.afm-journal.de

Genetically Controlled Iron Oxide Biomineralization in Encapsulin Nanocompartments for Magnetic Manipulation of a Mammalian Cell Line

Maria V. Efremova, Ulf Wiedwald, Felix Sigmund, Silviu-Vasile Bodea, Hendrik Ohldag, Thomas Feggeler, Ralf Meckenstock, Lorenz N. Panzl, Jeroen Francke, Irina Beer, Natalia P. Ivleva, Irina B. Alieva, Anastasiia S. Garanina, Alevtina S. Semkina, Franziska Curdt, Nicolas Josten, Sebastian Wintz, Michael Farle, Reinoud Lavrijsen, Maxim A. Abakumov, Michael Winklhofer, and Gil G. Westmeyer**

Magnetic nanoparticles have proven invaluable for biomechanical investigations due to their ability to exert localized forces. However, cellular delivery of exogenous magnetic agents often results in endosomal entrapment, thereby limiting their utility for manipulating subcellular structures. This study characterizes and exploits fully genetically controlled biomineralization of iron-oxide cores inside encapsulin nanocompartments to enable magnetic-activated cell sorting (MACS) and magnetic cell manipulation. The fraction of MACS-retained cells showed substantial overexpression of encapsulins and exhibited both para- and ferrimagnetic responses with magnetic moments of 10^{-15} A m^2 per cell, comparable to standard exogenous labels for MACS. Electron microscopy revealed that MACS-retained cells contained densely packed agglomerates of ≈30 nm iron oxide cores consisting of ultrafine quasicrystalline ordered nuclei within an amorphous matrix of iron, oxygen, and phosphorus. Scanning transmission X-ray microscopy, X-ray absorption spectroscopy, and Raman microspectroscopy confirmed that the iron-oxide species are consistent with ferric oxide (Fe_2O_3). In addition, the encapsulin-overexpressing MACS-retained cells can be manipulated by a magnetic needle and regrown in patterns determined by magnetic gradients. This study demonstrates that the formation of quasicrystalline iron oxide with mixed para/ferrimagnetic behavior in the cytosol of mammalian cells enables magnetic manipulation without the delivery of exogenous agents.

1. Introduction

The use of synthetic magnetic nanomaterials has a long history in biomechanical studies of cells.[1,2]

Fully genetic methods to generate biomagnetic structures would be desirable, but the only experimentally confirmed instances of genetically controlled magnetic materials in nature are found in so-called magnetosomes inside magnetotactic bacteria,[3–5] as extracellular iron biomineralization products in the teeth (radulae) of certain mollusks and vertebrates,[6–8] as well as in candidate magnetoreceptor structures of some vertebrates.[9]

Overexpression of ferritin, the most abundant iron-storing protein complex in mammalian cells, has been proposed as a biomagnetic handle.[10,11] However, calculations show that the magnetic properties of native ferritin, which contains the low-magnetization ferrihydrite $[FeO(OH)]_8[FeO(H_2PO_4)]$ are orders of magnitude too weak to support the proposed mechanisms.[12–14] Moreover, the

M. V. Efremova, F. Sigmund, S.-V. Bodea, L. N. Panzl, G. G. Westmeyer
Department of Bioscience of TUM School of Natural Sciences and TUM School of Medicine and Health
Technical University of Munich
Ismaninger Str. 22, 81675 Munich, Germany
E-mail: m.efremova@tue.nl; gil.westmeyer@tum.de

The ORCID identification number(s) for the author(s) of this article can be found under https://doi.org/10.1002/adfm.202418013

DOI: 10.1002/adfm.202418013

M. V. Efremova, F. Sigmund, S.-V. Bodea, L. N. Panzl, G. G. Westmeyer
Institute for Synthetic Biomedicine
Helmholtz Zentrum München
Ingolstaedter Landstr. 1, 85764 Oberschleissheim, Germany

M. V. Efremova, J. Francke, R. Lavrijsen
Department of Applied Physics and Science Education
Eindhoven University of Technology
PO Box 513, Eindhoven 5600 MB, The Netherlands

U. Wiedwald, R. Meckenstock, N. Josten, M. Farle
Faculty of Physics and Center for Nanointegration (CENIDE) Duisburg-Essen
University of Duisburg-Essen
Lotharstraße 1, 47057 Duisburg, Germany

ferritin cage is small (≈8 nm), holding only ≈4000 Fe atoms,[15] and is highly conserved, allowing for little modifications by bioengineering.[16,17] Li et al. coupled ferritin to micrometer-long Inkabox-PAK4 scaffolds, which enabled magnetic manipulation but only after iron-loading in vitro followed by cell uptake.[18] Another way to overcome the limitations of native ferritin is its reconstitution with magnetite Fe_3O_4, cobalt ferrite $CoFe_2O_4$, and other ferri/ferromagnetic iron oxide species ("magnetoferritin"),[19–21] but this is not possible in live cells.

A promising strategy for working with live cells is thus to identify genetically controlled nanocompartments that can facilitate the biomineralization of larger quantities of Fe oxides under local reaction conditions that can be tailored by bioengineering structural and enzymatic activities within the nanocompartment. This approach could enable the production of Fe biominerals with enhanced magnetic properties under physiological conditions for mammalian cells. We have previously shown that heterologous expression of an iron-biomineralizing encapsulin nanocompartment from *Myxococcus xanthus* in mammalian cells can enable retention by magnetic-activated cell sorting (MACS) and detection by magnetic resonance imaging.[22] These capabilities are enabled by an iron biomineralization process within self-assembling encapsulin protein shells driven by an encapsulated ferroxidase.[22,23] Nevertheless, the specific characteristics that differentiated the fraction of sorted cells from the remainder of the population were not examined.

Subsequently, we found that the encapsulin system from *Quasibacillus thermotolerans (Qt)* has a larger diameter (≈42 nm) and can more efficiently biomineralize iron when expressed in mammalian cells.[23,24] However, unlike iron-oxides from naturally occurring magnetic cells such as magnetotactic bacteria,[25,26] the biominerals formed in *Qt* encapsulins expressed in mammalian cells have not been characterized carefully.

In this study, we perform a detailed analysis and identification of iron oxide-filled *Qt* encapsulins expressed in MACS-retained cells with respect to their magnetic properties, subcellular distribution, ultrastructure, and chemical composition and show how these material properties can be used to pattern cell growth.

2. Results

2.1. Mammalian Overexpression of Iron-Accumulating Encapsulins

We first generated a construct that allows expression of the self-assembling encapsulin monomer from *Q. thermotolerans* with a FLAG tag ($QtEnc^{FLAG}$) and the corresponding ferroxidases (QtIMEF) via a 2A peptide. We also co-expressed the red fluorescent protein mScarlet-I via an internal ribosome entry site (IRES) for facile detection (Table S1, Supporting Information). Cellular uptake of ferrous iron was enhanced by co-expression of the iron importer $Zip14^{FLAG}$ (**Figure 1A**). After transient expression of the constructs for 24 h, ferrous ammonium sulfate was added to the medium for 48 h before cells were sorted on commercial MACS columns into "MACS-separated"; or ";MACS-retained" cells and "flow-through" cells that were not retained in the column. The cell fraction expressing all proteins listed above but not subjected to sorting will be further referred to as non-sorted cells. Additionally, we had a control population of HEK293T cells transfected with a plasmid encoding mScarlet-I protein and IRES only, which will be referred to as "no encapsulins" condition.

2.2. MACS of Encapsulin-Expressing Cells

A fraction of cells (1.77 ± 0.41%, mean ± SD, $n = 6$ independent experiments) expressing the encapsulin shell, ferroxidase, and the iron importer Zip14 were reliably retained on the magnetic sorting column when placed in the magnetic field (Figure 1B). However, when the same material was passed over the sorting column outside the magnetic field, only 0.20 ± 0.14% (mean ± SD) of cells were retained ($p = 0.0022$, Mann-Whitney test).

In a control experiment (Figure S1, Supporting Information), we expressed the $QtEnc^{FLAG}$ protein as an individual plasmid and replaced the DNA encoding QtIMEF or both QtIMEF and $Zip14^{FLAG}$ with sequences coding for fluorescent proteins (mEos4b targeted to the encapsulin lumen (DD-mEos4b-QtSig),[22] and eYFP, respectively). In these control conditions,

H. Ohldag, T. Feggeler
Advanced Light Source
Lawrence Berkeley National Laboratory
6 Cyclotron Rd, Berkeley, CA 94720, USA
H. Ohldag
Department of Material Sciences and Engineering
Stanford University
496 Lomita Mall, Stanford, CA, USA
H. Ohldag
Department of Physics
University of California Santa Cruz
1156 High Street, Santa Cruz, CA 95064, USA
T. Feggeler
Department of Physics
University of California Berkeley
366 Le Conte Hall, Berkeley, CA 94720, USA
I. Beer, N. P. Ivleva
Chair of Analytical Chemistry and Water Chemistry
Institute of Water Chemistry
Department of Chemistry
TUM School of Natural Sciences
Technical University of Munich
Lichtenbergstraße 4, 85748 Garching, Germany
I. B. Alieva
A.N. Belozersky Institute of Physical and Chemical Biology
Lomonosov Moscow State University
Leninskiye Gory 1, building 40, Moscow 119234, Russian Federation
A. S. Garanina, M. A. Abakumov
National University of Science and Technology «MISIS»
Leninskiy Prospekt 4, Moscow 119049, Russian Federation
A. S. Semkina, M. A. Abakumov
Department of Medical Nanobiotechnology
Russian National Research Medical University
Ulitsa Ostrovityanova 1, Moscow 117997, Russian Federation
F. Curdt, M. Winklhofer
Institut für Biologie und Umweltwissenschaften
Carl von Ossietzky Universität Oldenburg
Ammerländer Heerstr. 114–118, 26129 Oldenburg, Germany
S. Wintz
Max Planck Institute for Intelligent Systems
Heisenbergstraße 3, 70569 Stuttgart, Germany
M. Winklhofer
Forschungszentrum Neurosensorik
Carl von Ossietzky Universität Oldenburg
Carl-von-Ossietzky-Straße 9, 26129 Oldenburg, Germany

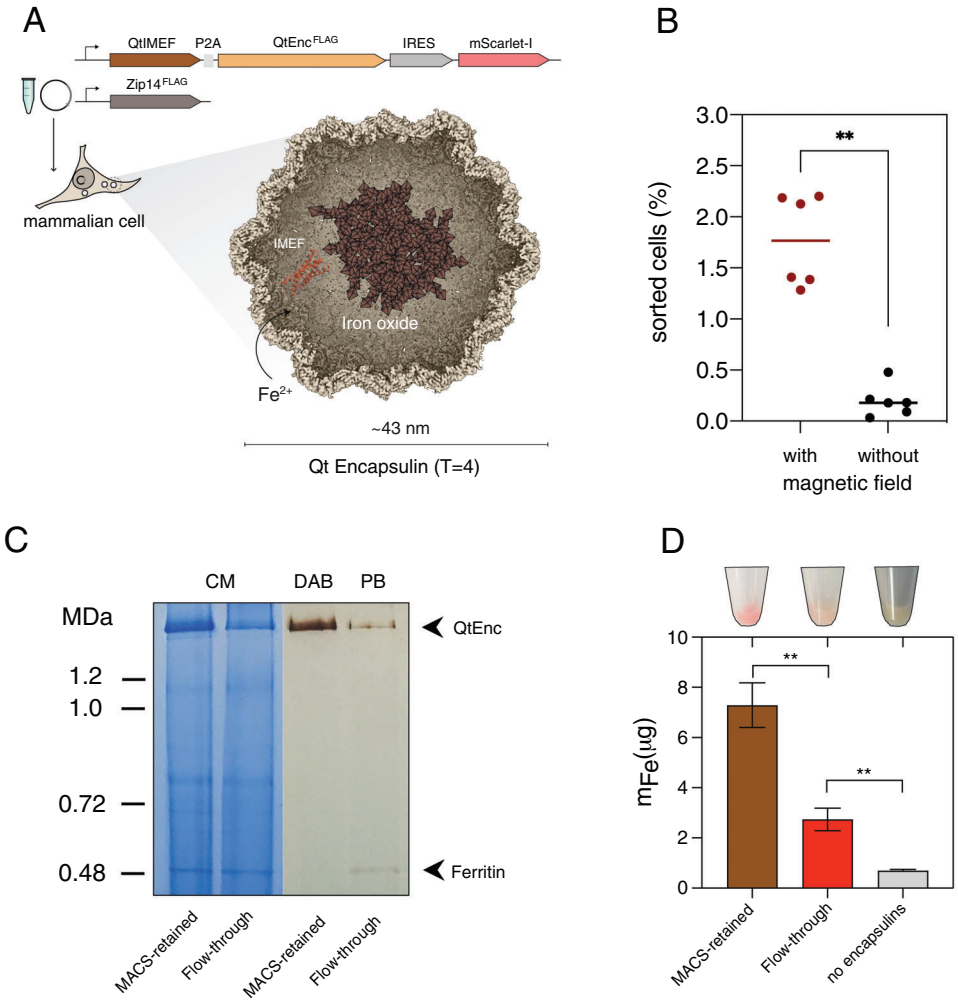

Figure 1. Magnetic-activated cell sorting of mammalian cells overexpressing iron-accumulating encapsulins. A) Scheme showing the bicistronic expression construct encoding the ferroxidase (IMEF) from *Q. thermotolerans* (QtIMEF) together with the FLAG-tagged encapsulin monomer (via P2A), which self-assembles into the protein shell (QtEnc^{FLAG}), and the red fluorescent protein mScarlet-I (via an IRES site). The iron transporter Zip14^{FLAG} was co-expressed from a separate plasmid, and transfected HEK293T cells were cultivated in the medium supplemented with 2 mM ferrous ammonium sulfate (FAS) for 24 h. B) Comparison of the magnetic sorting efficacy of HEK293T cells expressing QtEnc^{FLAG} with the ferroxidase IMEF and the iron transporter Zip14^{FLAG} in the commercial columns for magnetic-activated cell sorting (MACS) with or without applying a magnetic field to control for merely mechanical retention on the columns. The cell medium was supplemented with 2 mM FAS for 24 h. Combining the expression of the above-mentioned proteins and applying a magnetic field allowed for the isolation of 1.77 ± 0.41% (mean values ± SD) of the whole HEK293T cell population. Without applying a magnetic field, the sorting efficiency was 0.20 ± 0.14% (mean values ± SD). Data points represent $n = 6$ independent transfections and experiments for each data set. Statistical analysis was performed by the Mann-Whitney test (** corresponds to p-value < 0.01). C) Coomassie-stained Blue Native PAGE (CM) and DAB-enhanced Prussian blue-stained (DAB PB) gels loaded with whole lysates of either MACS-retained cells or flow-through cells of ($4.65 \cdot 10^5$ cells each) showing the band of the native QtEnc^{FLAG} protein and ferritin. D) The mass of Fe contained in the pellets of MACS-retained cells, flow-through cells, and control wild-type cells supplemented with 2 mM FAS (7.4×10^6 cells each) was determined by inductively coupled plasma mass spectrometry (ICP-MS). All numbers are plotted as mean values ± SD ($n = 3$). Statistical analysis was performed by an unpaired t-test (** corresponds to p-value < 0.01). Insets show photographs of the cell pellets in test tubes after the magnetic sorting. The red color of the pellets is related to the expressed mScarlet-I and possibly the iron content in the cells.

only 0.13 ± 0.20% and 0.12 ± 0.11% were retained in the magnetic field. A statistically significant difference ($p = 0.0047$ and $p = 0.0182$, respectively, $n = 6$, Kruskal-Wallis test with Dunn's multiple comparisons) was found with respect to 1.37 ± 0.20% cells expressing QtEnc^{FLAG}, QtIMEF, and Zip14^{FLAG} (Figure S1, Supporting Information) sorted in the magnetic field.

Whole-cell lysates of MACS-retained and flow-through cells were then loaded in identical volumes onto native gels stained with either Coomassie (CM) or iron-selective Prussian blue (PB), which can be enhanced with diaminobenzidine (DAB-PB) (Figure 1C). For both MACS-retained cells and flow-through cells, a band running above the highest marker band was visible by CM, consistent with the presumed molecular weight of fully assembled QtEnc^{FLAG} nanocompartments (≈9.6 MDa). The CM band and DAB PB signal for QtEnc were stronger in the MACS-separated cells. However, a DAB PB band for endogenous

ferritin (≈0.5 MDa molecular weight) was detectable only in flow-through cells and not in MACS-separated cells, while the CM signals were similar.

Next, we determined the cellular iron content using ICP-MS (Figure 1D). We observed an almost 3-fold increase in iron content of MACS-separated versus flow-through cells (7.29 versus 2.74 μg_{Fe} per equal number of cells, $p = 0.0014$, $n = 3$, unpaired t-test), which still had a substantially elevated amount of iron compared to non-transfected cells (0.69 μg_{Fe}, $p = 0.0015$, $n = 3$, unpaired t-test). The MACS-separated cell pellet was also more intensely stained red by the co-expressed m-Scarlet, indicating that magnetic sorting selects for highly overexpressing cells.

We tested for a possible cytotoxic effect of $QtEnc^{FLAG}$, QtIMEF, and $Zip14^{FLAG}$ expression and iron biomineralization using the LDH-Glo assay, which measures the release of lactate dehydrogenase (LDH) into the culture medium as a proxy for cell membrane damage. The analysis showed no significant difference in cell viability between 0–1.5 mM FAS (p-values > 0.05, Kruskal-Wallis test with Dunn's multiple comparisons), but there was a small decrease in cell viability to 90.1 ± 7.6% for 2 mM FAS ($p = 0.0448$, $n = 6$, Kruskal-Wallis test with Dunn's multiple comparisons, Figure S2, Supporting Information).

2.3. Magnetic Characterization

We applied field-dependent vibrating sample magnetometry (VSM) and ferromagnetic resonance/electron paramagnetic resonance (FMR/EPR) to quantify the magnetic properties of MACS-separated cells in comparison to flow-through cells, non-sorted cells, and cells that only expressed the fluorescent protein mScarlet-I ("no encapsulins").

We first obtained magnetic hysteresis loops of the MACS-separated cells (batch 1) at $T = 200$ K after cooling in a zero field and compared them with three controls (**Figure 2A**).

Diamagnetic and paramagnetic background contributions were removed, as described in the Materials & Methods section. Only the cells separated by MACS exhibited a magnetic hysteresis loop with a total sample saturation magnetic moment of $\approx 4.0 \times 10^{-9}$ A m^2. This value is more than four times higher than the established detection limit, as evidenced by three additional samples showing magnetic responses at the noise level (1.0×10^{-9} A m^2). The right y-axis in Figure 2A expresses the normalized magnetic moment per amount of Fe in the ferrimagnetic state, as described below in the detailed analysis of the magnetic response by FMR. We determined a saturation magnetization $M_s = 56.0$ A m^2 kg^{-1}.

Two exemplary hysteresis loops of the MACS-separated cells (batch 1) at $T = 50$ K and $T = 200$ K (Figure 2B) reflect the decreasing magnetization with temperature. The magnetization per magnetically sorted cell at 200 K is $\approx 1 \times 10^8$ μ_B (right scale). It is important to note that slight asymmetries are due to the small ferrimagnetic signal overlaid with additional paramagnetic and diamagnetic signals. This becomes clearer by examining the sample response after subtracting the high-field diamagnetic susceptibility χ_{HF} in Figure S3, Supporting Information. We obtain a strong and saturated paramagnetic signal ($\mu = 2.8 \times 10^{-7}$ A m^2) at $T = 3$ K and B = 5 T (Figure S3A, Supporting Information), which is almost 2 orders of magnitude larger than the ferrimagnetic response in Figure 2A, and decays strongly with temperature. Above $T = 50$ K, this Langevin paramagnetism gives a strictly linear background as a function of external field on top of the ferrimagnetism, indicating that the encapsulin nanoparticles exhibit both para- and ferrimagnetic responses, and the temperature range from 50–200 K is the best window to extract

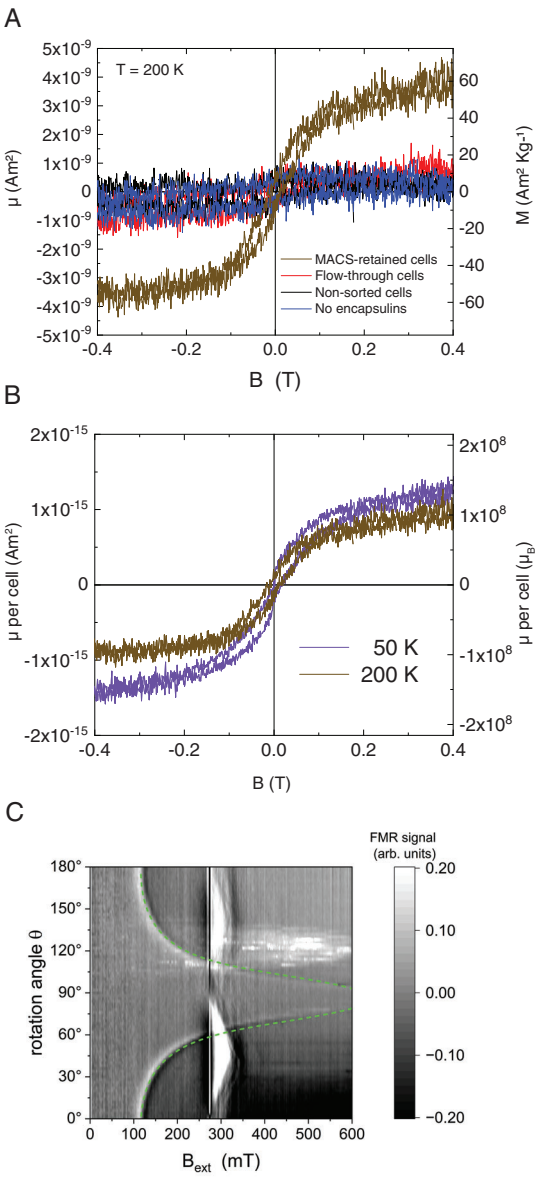

Figure 2. Vibrating sample magnetometry (VSM) and ferromagnetic resonance (FMR). A) VSM at $T = 200$ K showing hysteresis loops of the pellets comprising ≈4 × 10^6 HEK293T cells co-expressing the $QtEnc^{FLAG}$, QtIMEF, mScarlet-I, and $Zip14^{FLAG}$ from MACS-retained, flow-through, and non-sorted cell fractions as well as from HEK293T cells expressing the fluorescent protein mScarlet-I ("no encapsulins" condition). The cell medium was supplemented with 2 mM FAS for 48 h. The scale on the right applies to MACS-retained cells only. B) Magnetic moment per cell at $T = 50$ K and 200 K after zero-field cooling. C) Angular-dependent FMR at 9.412 GHz and $T = 200$ K after field cooling in B = 1 T at $\Phi = 0°$ from the liquid state. The green dashed curve indicates an angular-dependent FMR with uniaxial anisotropy.

information about long-range ferrimagnetic order in the encapsulin nanoparticles. The high-field susceptibility χ_{HF} decreases from ≈3.0 × 10^{-8} m^3 g_{Fe}^{-1} (2.4 × 10^{-3} emu g_{Fe}^{-1} Oe^{-1}) at 3K to 2.5 × 10^{-8}•m^3 g_{Fe}^{-1} (2.0 × 10^{-4} emu g_{Fe}^{-1} Oe^{-1}) at 200 K (Figure S3B, Supporting Information, data shown after removal of diamagnetism from the cell matrix and water). For better comparison with the literature, we give χ_{HF} in SI and cgs units here.

Additionally, we assessed the reproducibility of the magnetic responses on a separate cell sample produced six months after the one presented in Figure 2A,B. We obtained highly comparable hysteresis curves at T = 200 K from two distinct sample batches (Figure S3C, Supporting Information).

For further proof of long-range magnetic order, we employed temperature- and angular-dependent FMR on the same sample, which was cooled down from 300 to 50 K in B = 1 T at an angle Φ = 0°. FMR/EPR measurement at T = 200 K and T = 50 K (Figure 2C and Figure S3D,E Supporting Information). We observed a major angular-independent EPR line at 312 mT (g-factor of 2.15) and EPR lines at B = 210 mT (g = 3.2) and B = 155 mT (g = 4.3) with much lower intensities. To highlight the more interesting ferromagnetic component visible in the angular-dependent FMR line with uniaxial anisotropy (green dashed line), we have subtracted the strong EPR references line. The resulting demagnetization field varies between B = 115 mT for Φ = 0° and 330 mT for Φ = 90°. The FMR line can be identified by the broader peak-to-peak linewidth. The amplitude of the FMR is, however, only about 5% of the main EPR line at B = 312 mT and linewidth ΔB_{pp} = 15 mT. We fitted the FMR angular dependencies, assuming rod-like assemblies of encapsulin nanoparticles or their preformed aggregates before subsequent freezing (green broken lines in the color plots, cf. detailed information in the discussion section). Under the assumption that the angular dependence of the FMR line solely depends on the magnetization of the encapsulin nanoparticles and their uniaxial symmetry, we extracted a magnetization of the ferrimagnetic component of 280 kA m^{-1} at 200K with uncertainties ≈±25%. We used this estimate to rescale the magnetization of the hysteresis loops in Figure 2A.

2.4. Intracellular Distribution of Iron-Accumulating Encapsulins

The subcellular distribution of iron-oxide-filled encapsulins was characterized using low-magnification brightfield transmission electron microscopy (TEM). Similar to our previous work,[23] $QtEnc^{FLAG}$ co-expressed with QtIMEF and $Zip14^{FLAG}$ produced strong contrast in TEM micrographs due to the electron-dense iron-rich cores inside the protein shells (**Figure 3**).

We conducted automated semantic segmentation of the iron-oxide cores (Figure 3A). We then quantified that MACS-retained cells contained ≈5 times more cores per cell area than the flow-through cells not captured by the MACS column, consistent with the analyses of iron abundance in Figure 1C,D (Figure 3B–D). Interestingly, we found that about half of the iron-oxide cores (51 ± 23%) in MACS-retained cells were clustered inside cytosolic agglomerates, covering 10 ± 7% of the cell area seen in the TEM cross-section. In flow-through cells not retained on the MACS columns, only a very variable fraction of the iron cores of 18 ± 26% was found inside aggregates, covering a significantly smaller cell area of 1 ± 2% ($p < 0.001$, n = 92, Dunn's multiple comparison after Kruskal-Wallis test).

To further control for potential confounding variables, we also used fluorescence-activated cell sorting (FACS), to isolate the top 2% of cells overexpressing mScarlet-I (Figure S4, Supporting Information), which contained about half of the iron oxide cores found in the MACS-retained cells. However, only 2.6 ± 8% of these cores were found in aggregates. In the MACS-retained cells, we also found multiple examples of aggregates with tightly packed iron cores, which in some instances showed a sub-organization in a chain- or rod-like alignment (Figure 3E). We measured the diameter of the iron-oxide cores to be 31 ± 3 nm and the outer diameter of empty encapsulin protein shells as 40 ± 3 nm (light blue outlines in Figure 3E), in line with cryo-TEM data we reported earlier and maximum filling of the encapsulin lumen.[23] The center-to-center distance between adjacent cores was 43 ± 2 nm (Figure 3F), just slightly larger than the shell diameter, thus indicating close packing of the spheres (Figure 3F). Besides the cytosolic localization, we also observed encapsulin ensembles in the endolysosomes and autophagosomes in all three conditions (Figure S5, Supporting Information).

2.5. Crystallinity and Elemental Analysis of Encapsulin Particles

To analyze the crystalline structure of encapsulin cores in the ultrathin cell sections, we performed high-angle annular dark-field (HAADF) imaging in scanning transmission electron microscopy (STEM) mode. The HAADF-STEM image of the encapsulin nanoparticles in MACS-separated cells (**Figure 4**A,B) demonstrates the low crystallinity of particles, i.e., the absence of long-range order, in line with the corresponding Fast Fourier Transform image (FFT image, inset) not showing any ring patterns either. Nevertheless, on the single-particle level (Figure 4C), one can see that the amorphous matrix of the encapsulin core includes ultrafine nuclei with a short-range crystalline order (10-20 atomic columns) indicated by dark red arrows (Figure 4C, insets).

According to energy-dispersive X-ray spectroscopy (EDX) mapping, iron, phosphorus, and oxygen represent the main components of encapsulin cores in MACS-separated cells (Figure 4D). Analysis of the EDX linear profiles of iron and phosphorus (Figure 4E,F) reveals a large variation in the average Fe:P ratio from particle to particle. To check whether this ratio also depends on the agglomeration state of encapsulins, we performed a quantitative analysis of Fe and P content in 10 different areas of cells inside or outside of aggregates (insets in Figure S6A, B, Supporting Information). Each area contained 4–5 electron-dense encapsulin cores and was randomly chosen. We determined the Fe:P atomic ratio R_{at} = 1.6±0.1 (mass ratio R_{mass} of 2.9±0.2) for the encapsulins in the aggregates, which was significantly higher than R_{at} = 1.3±0.1 (R_{mass} = 2.4±0.2) for the encapsulins homogeneously dispersed in the cytoplasm (p-value < 0.0001, Mann-Whitney test, n = 10, Figure S6C and Tables S2 and S3, Supporting Information). A center-surround pattern was discerned in some aggregated (Figure S6D, Supporting Information) and dispersed (Figure S6E, Supporting Information) encapsulin particles, with the core and shell predominantly containing iron or phosphorus, respectively.

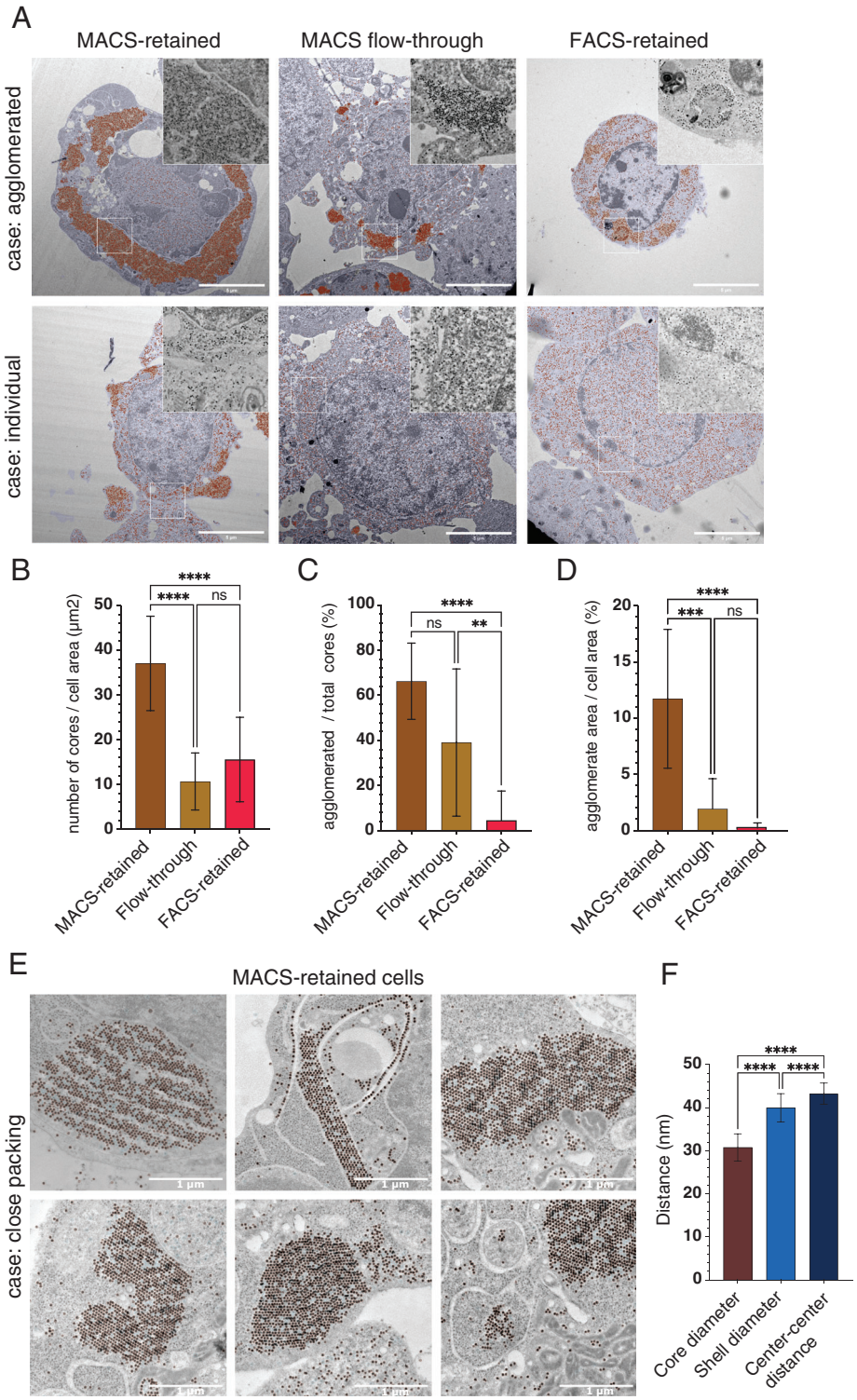

Figure 3. Subcellular distribution of iron-oxide-filled encapsulins. A) Representative bright-field TEM images for the three experimental conditions and cases of cytosolic agglomerated or individual encapsulins with the zoom-ins to the enboxed regions as insets. The transparent overlays show the automated segmentations of encapsulin cores (red), the regions identified as agglomerates (orange), and respective cell areas (blue) to quantify B)-D). B) The abundance of iron-oxide cores. C) The fraction of encapsulins inside an agglomerate. D) The relative cell area covered with agglomerates. E) TEM micrographs at a higher magnification showing examples of densely packed encapsulins in MACS-retained cells with segmentation outlines for iron-oxide cores in red and empty encapsulin shells in light blue. F) Quantifications of the diameter of the iron-oxide core (31 ± 3 nm), the outer diameter of the encapsulin protein shell (40 ± 2 nm), and center-to-center distance of the iron oxide cores (43 ± 2 nm). Significant comparisons are from a Kruskal-Wallis test with Dunn's multiple comparison tests (*$P < 0.05$; **$P < 0.01$; ****$P < 0.0001$).

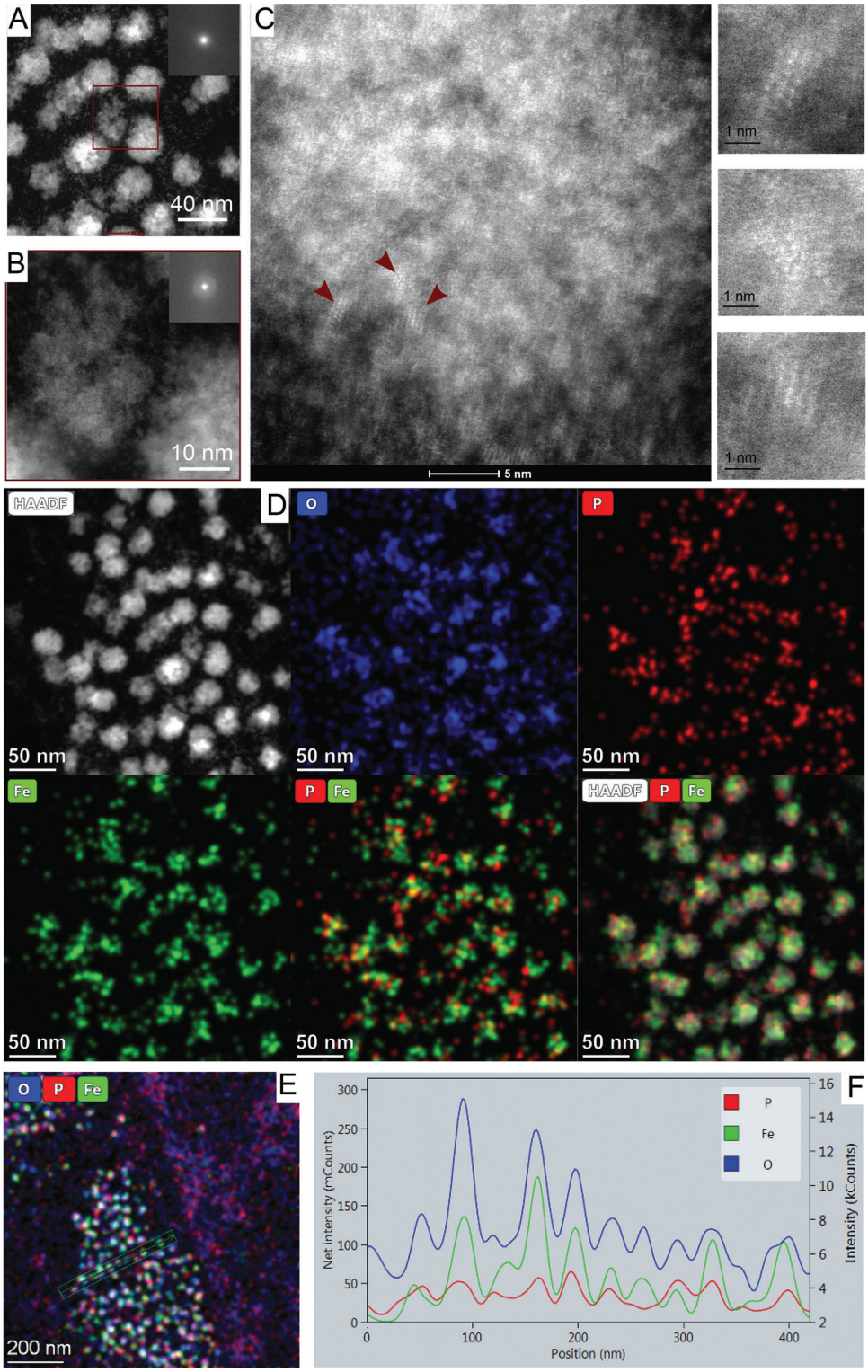

Figure 4. Structural and elemental analysis of the encapsulins in MACS-retained cells. High-resolution TEM (HRTEM), high-angle annular dark-field-scanning transmission electron microscopy (HAADF-STEM), and energy-dispersive X-ray spectroscopy (EDX) investigations reveal the composition and local quasicrystalline order in the electron-dense cores of encapsulin nanoparticles in MACS-retained HEK293T cells. A), B) HAADF-STEM images of the aggregate of encapsulin electron-dense cores and Fast Fourier Transform images (FFT, insets) demonstrating the amorphous structure of the nanoparticles. C) HRTEM image showing nanocrystalline domains (pointed by dark red arrows and magnified in the insets) in the amorphous matrix of a single encapsulin particle. D), E) EDX-elemental mapping of the electron-dense encapsulin cores primarily containing iron, oxygen, and phosphorus. F) EDX scan through the designated line in (E) showing the variability of the Fe/P ratio in encapsulin nanoparticles.

We also analyzed the composition of the encapsulin particles formed in the flow-through cells (Figure S7, Supporting Information). Compared to the encapsulin particles in MACS-separated cells, electron-dense cores in the flow-through cells are more phosphorus-rich with an average R_{at} = 1.1±0.2 and corresponding R_{mass} = 2.0±0.3, meaning that the P content is significantly higher than in the aggregated encapsulins in the MACS-sorted cells (p-value < 0.0001, Kruskal-Wallis test with Dunn's multiple comparisons, n = 10, Table S4, Supporting Information).

Finally, we tested whether the phosphorus content of the encapsulated biomineral changes when culturing the cells in DMEM without phosphates and FBS as the only source of P (low P cells), keeping all other experimental conditions unchanged. The cells were then magnetically sorted using the same procedure as before, and the sorted fraction was investigated by TEM, HAADF-STEM, and EDX (Figure S8 and Table S5, Supporting Information). Encapsulins in low P cells had a Fe content (1.9±0.2 and 3.5±0.4 for atomic and mass Fe:P ratio, respectively), which was significantly higher than the dispersed encapsulins in MACS-sorted cells and the flow-through cells, both cultured in a standard DMEM (p = 0.0004 and p < 0.0001, respectively, Kruskal-Wallis test with Dunn's multiple comparisons, n = 10). Nevertheless, no significant difference was found compared to the aggregated encapsulins in MACS-sorted cells cultured in a standard DMEM (p = 0.4224, Kruskal-Wallis test with Dunn's multiple comparisons, n = 10), and the crystalline structure of particles remained (predominantly) amorphous.

2.6. Characterization of Iron-Oxide Species in MACS-Separated Cells

Given that high-angle annular dark-field scanning transmission electron microscopy (HAADF-STEM) revealed the absence of long-range crystalline order of iron-oxide cores within encapsulins, we subsequently sought to gain insight into the local coordination and chemical state of the iron atoms. To this end, we analyzed ultrathin sections of MACS-retained cells using synchrotron radiation-assisted scanning transmission X-ray microscopy (STXM) and X-ray absorption spectroscopy (XAS). We obtained an XAS spectrum at Fe L_3-edge from an ultrathin section area containing an encapsulin particle aggregate as detected by STXM (**Figure 5**A,B).

Subsequently, we conducted multiple peak regression analyses using spectra obtained from reference iron-oxide species on the same system.[27] Applying a linear mixing model with ferric (Fe_2O_3) and ferrous oxide (FeO) end members, we achieved a good fit for a mixture of 85% Fe_2O_3 and 15% FeO (Figure 5A), corresponding to a molar ratio of ferric to ferrous iron of 5.1:1 (while stoichiometric magnetite would have 2:1). A slightly better fit was obtained when mammalian ferritin with its ferrihydrite-like core phase was used as ferric end member (71% of ferritin versus 29% of FeO, see Figure 5C). These findings suggest the presence of a mixed valence iron oxide within the encapsulin cores.

In contrast, ferric iron phosphate ($FePO_4$) can be excluded as a principal phase because an energy shift of ≈0.5 eV toward higher energies relative to Fe_2O_3 can be observed, even though the overall shape of the XAS curve is similar to the latter also showing a "shoulder" between 711 and 714 eV, which is absent in the Fe_2O_3 spectrum (Figure 5D). Magnetite (Fe_3O_4) can also be excluded as a principal phase because of the energy shift of ≈0.3 eV toward lower energies relative to Fe_2O_3 and a different curve shape and width for the range of 708–709 eV (Figure 5D).

Since several ferric oxide/hydroxide candidate minerals could be consistent with the XAS spectra, a second technique was needed to constrain the nature of the compound in terms of composition and crystal structure. To this end, we used Raman spectroscopy in live MACS-separated cells re-plated on the substrate after the sorting procedure. We selected a region of interest (ROI) in an aggregate of encapsulin nanoparticles (detectable as a micrometer-sized contrasted area across a wide range of Z-positions). We also selected a reference ROI in the cytoplasm, which appeared as a homogeneous area in the cell without a visible contrast and served as a negative control in our experiment. We acquired the Raman spectra in the 50–3500 cm^{-1} range containing all characteristic peaks of a living cell (Figure S9A, Supporting Information), while the interval between 600 and 750 cm^{-1} had the lowest background, allowing for the primary phase identification of iron oxides in encapsulins (Figure 5E). We detected a band at ≈700 cm^{-1} from the encapsulin aggregate ROI that was not apparent in the free cytoplasm (Figure 5E, inset).

According to the literature,[28] the position of the band at ≈700 cm^{-1} is typical for maghemite (γ-Fe_2O_3), inorganic ferrihydrite, and ferritin-derived ferrihydrite, e.g. $[FeO(OH)]_8[FeO(H_2PO_4)]$. In contrast, the strongest Raman mode of magnetite[29,30] would be expected at lower wavenumbers (670 cm^{-1}). The characteristic Raman line of hematite (α-Fe_2O_3) at 613 cm^{-1}[29,30] was not detectable. A peak at ≈720 cm^{-1}, consistent with akaganeite (β-FeOOH),[29,30] was observed in our reference sample of dextran-coated akaganeite particles (Figure S9B, Supporting Information), but not clearly discernable in the measurement from the MACS-retained cells.

Summarizing the materials characterization, we identified 1–3 nm-sized nanocrystalline structures in a quasi-amorphous P-rich matrix within encapsulin cores in MACS-separated cells by HRTEM. Thus, based on the obtained XAS and Raman spectra in combination with the magnetic measurements, the quasicrystalline phase is consistent with maghemite (γ-Fe_2O_3). Another candidate material could be ordered ferrihydrite ($Fe_{10}O_{14}(OH)_2$), in which ferric ions in both octahedral and tetrahedral sites can give rise to ferrimagnetism (up to 58.5 A m^2 kg^{-1}) that persists up to 400K.[31] Since ferrihydrite does not precipitate directly but only after several hours of heating at 175 °C,[31] it, however, seems unlikely that ordered ferrihydrite is present in encapsulin cores.

2.7. Manipulation and Patterning of Magnetic Cells

Finally, we assessed how well our genetically engineered magnetic cells can be magnetically manipulated with higher spatial precision. We thus attached a permalloy needle to the stack of two disk-shaped permanent NdFeB magnets and a permalloy cone mounted on a micromanipulator, generating a high gradient field for magnetic attraction. The geometry of the permalloy tip and the calculated maps of magnetic induction and its gradient field are shown in Figure S10, Supporting Information. The permalloy tip with magnetizing NdFeB permanent magnets (Figure S10A, Supporting Information) has an induction of

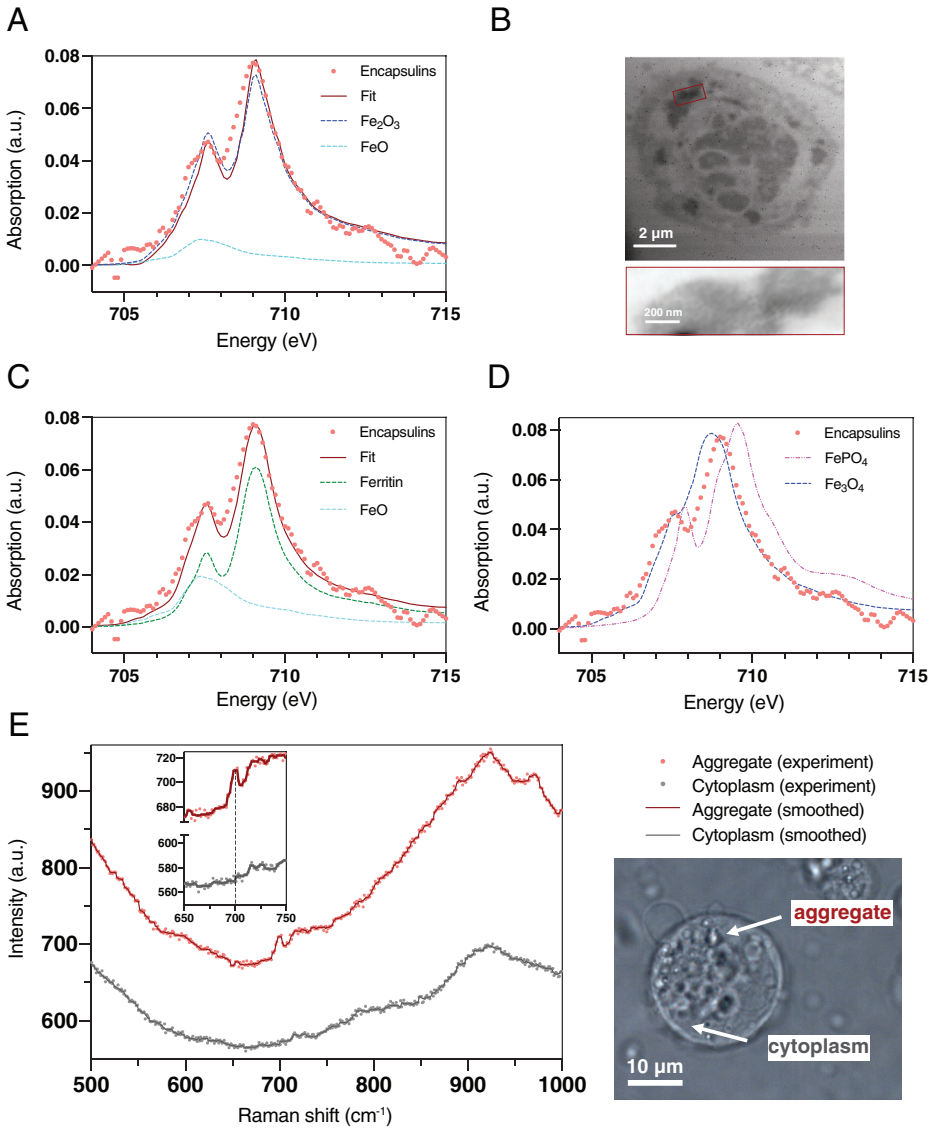

Figure 5. Local coordination of Fe in the electron-dense encapsulin cores in MACS-retained cells. A)-D) X-ray absorption spectrum (XAS) in the Fe $2p^{3/2}$ to 3d excitation region ("L3 edge") probed from an aggregate of encapsulin nanocompartments within an ultrathin cell section in the synchrotron radiation-assisted scanning transmission X-ray microscopy (STXM). A) Data points (pale red dots) are fit by multiple peak regression (solid dark red curve) with Fe_2O_3 as the main component (85% fitting proportion, dashed blue curve) and FeO as the minor component (15% fitting proportion, dashed cyan curve). B) STXM images of the ultrathin cell section where encapsulin aggregates are identified (top) with a close-up of where the XAS was registered, and individual encapsulin nanoparticles can be distinguished (bottom). C) Data points (pale red dots) are fit by multiple peak regression (solid dark red curve) with the ferritin from equine spleen (Sigma) as the main component (Ferritin, 71% fitting proportion, dashed green curve) and FeO as the minor component (29% fitting proportion, dashed cyan curve). D) Data points (pale red dots) are superimposed with a reference $FePO_4$ spectrum (dashed magenta curve) and Fe_3O_4 spectrum (dashed blue curve). E) Raman spectra of live MACS-retained cells (acquired 24 h post-replating on the substrate after the sorting procedure). Spectra are shown for two subcellular regions (see microscope image on the right), an aggregate of encapsulin nanoparticles (dark red curve, pale red dots), and free cytoplasm (dark gray curve, pale gray dots). The inset shows a close-up of the spectra between 650 and 750 cm^{-1}. The peak at 700 cm^{-1} apparent in the spectrum obtained in the encapsulin aggregate is indicative of $Fe(III)O_4^{3-}$ in maghemite or ferritin. All reference X-ray absorption spectra were acquired at the same beamline. X-ray absorption spectra of Fe_2O_3, FeO, Fe_3O_4, and $FePO_4$ were reported previously.[27]

0.93 T (Figure S10B, C, Supporting Information). The gradient field at the tip is 2.9×10^4 T m^{-1} and decays fast in x- and y- directions as shown in Figure S10D, Supporting Information. We immersed this needle in the suspensions of MACS-separated, flow-through, non-sorted, or control cells (expressing mScarlet-I only) in DPBS and recorded the video of the needle tip capturing the fluorescent signal of mScarlet-I (in RFP channel) that was co-expressed via DNA constructs in all experimental cells (Videos S1–S4, Supporting Information).

Immediately after the needle was immersed in the suspension of MACS-separated cells, we observed the attraction of cells to the needle in a ≈50 µm radius around the tip (**Figure 6A**, top

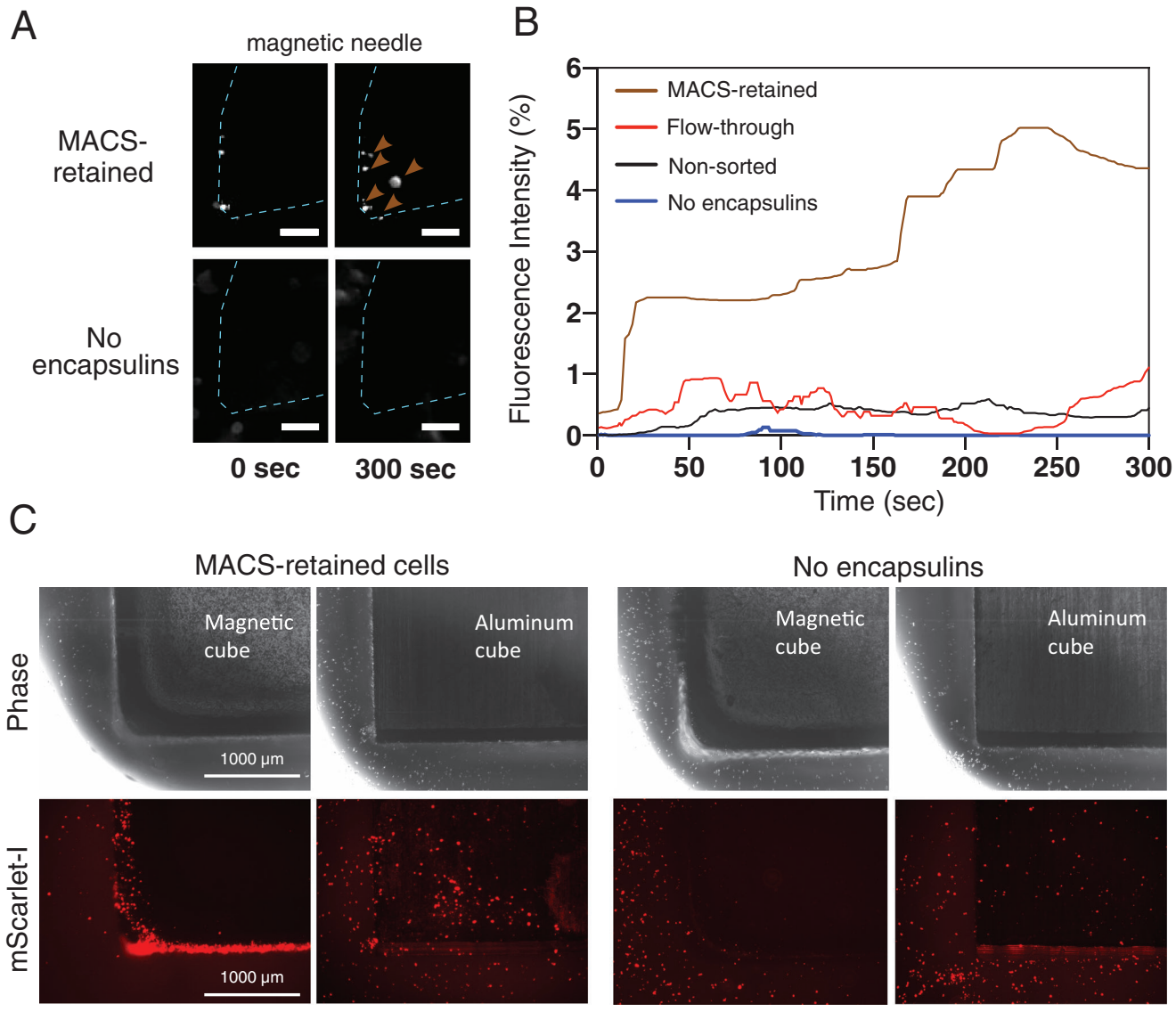

Figure 6. Manipulation of MACS-retained cells in a magnetic field. A permalloy magnetic needle attached to a permanent NdFeB magnet with an induction of 0.93 T at its tip was immersed into cell suspensions (1×10^5 cells mL^{-1}) from cells expressing the encapsulin system (QtIMEF-P2A-QtEnc^{FLAG}-IRES2-mScarlet-I and Zip14^{FLAG}) or controls after growth for 48 h at 2 mM FAS. A) Two exemplary frames at 0 s and 300 s, showing accumulation of fluorescence cells at different depths (brown arrowheads) on the tip of a needle (light blue outline) for MACS-retained cells (Video S1A, Supporting Information) compared to cells expressing mScarlet-I only ("No encapsulins" condition, Video S4A, Supporting Information). The scale bar represents 200 µm. B) Time courses of the fluorescence intensity profile for MACS-retained, flow-through, non-sorted, and no encapsulin cells during 300 s magnetic manipulation obtained from Videos S1A–S4A, Supporting Information, respectively. C) Phase contrast images (top row) and fluorescence microscopy images (bottom row) of MACS-retained cells and "No encapsulins" cells acquired 24 h after their replating on cell culture dishes, in which either a permanent NdFeB magnetic cube or an aluminum cube of identical dimensions were placed. The scale bar represents 1000 µm.

row). In contrast, control cells expressing mScarlet-I only showed lower efficiency and speed of attraction (Figure 6A, bottom row). Besides the qualitative observations, we also quantified the total fluorescence signal and its time-dependent accumulation at the needle tip for all tested cells (Figure 6B; Videos S1–S4, Supporting Information). MACS-separated cells showed ≈10x increase of the total fluorescence during 5 mins of observation (from 0.5% to 5% of the normalized value). In contrast, the signal of the flow-through, non-sorted, and control cells showed low to no obvious accumulation in the same period.

Finally, we studied the efficiency of magnetic cell manipulation in a longer time frame. MACS-separated and flow-through cells were replated on cell culture dishes immediately after the sorting procedure and compared to non-sorted cells and cells not expressing encapsulins. Subsequently, either a cubic permanent NdFeB magnet or an aluminum cube of identical dimensions was positioned on the cell culture dish. Epifluorescence microscopy of the culture dishes 24 h post-replating (Figure 6C) showed an accumulation of MACS-separated cells at the edges of the magnetic but not the aluminum cube, in line with the effect of

Table 1. Characterization of iron-containing particles in MACS-retained cells obtained from the analytical pipeline.

Parameter, source in the text	Measurement technique	Value extracted
Saturation magnetization of ferrimagnetic particles (M_s), Figure 2A	Overview of VSM (magnetic saturation), FMR	56.0 A m^2 kg^{-1}
Average magnetic moment per cell (μ_{cell}), Figure 2B	Overview of VSM (magnetic saturation)	10^{-15} A m^2
Estimate of the total mass of ferrimagnetic Fe per cell ($m_{Fe,ferri}$)	VSM (detailed analysis)	1.65×10^{-14} g
Estimate of the total mass of paramagnetic Fe per cell ($m_{Fe,para}$)	VSM (detailed analysis)	1.45×10^{-13} g
Total Fe mass per cell (m_{Fe}), Figure 1D	ICP MS	8.9×10^{-13} g
Diameter of iron-oxide core	TEM	31 ± 3 nm

magnetic gradients and controlling for any effects of the metallic cubes on cell growth independent of magnetic fields. In comparison, control cells and flow-through cells (Figure S11, Supporting Information) showed no obvious enrichment at the edges of the cubes. We confirmed that cells were viable post-replating, as indicated by the absence of a DAPI signal in their nuclei in a separate staining experiment (Figure S12, upper panel, Supporting Information), but fluorescence from the cell membrane permeable Hoechst dye (Figure S12, lower panel, Supporting Information).

3. Discussion

This study presents a comprehensive analysis of the results of genetic control of iron biomineralization inside encapsulins overexpressed in mammalian cells. Within the magnetically sorted cell fraction, we discovered encapsulins that contained ultrafine (1-3 nm-sized) quasicrystalline ferric oxide/hydroxide cores embedded within an amorphous iron-oxide-phosphorous matrix, exhibiting ferrimagnetism and paramagnetism.

MACS isolated 1–2% of cells exhibiting the highest encapsulin protein expression and iron load in $QtEnc^{FLAG}$ nanoshells when the ferroxidase QtIMEF and the iron importer $Zip14^{FLAG}$ were co-expressed, and the MACS columns were positioned within the magnetic field (Figure 1).

According to the DAPI/Hoechst staining, the cell membrane integrity of MACS-separated cells after replating was not compromised (see Figure S12, Supporting Information). However, a slight decrease in cell viability was observed in cells that were transduced with QtIMEF-P2A-$QtEnc^{FLAG}$-IRES-mScarlet-I and $Zip14^{FLAG}$, and supplemented with 2 mM FAS, as measured by LDH-Glo assay (Figure S2, Supporting Information). While we worked with a short iron supplementation of only 48 h during transient expression, future experiments may explore longer durations of iron administration in cell lines with chromosomally integrated encapsulin constructs.

Using VSM, we determined the average magnetic moment of the MACS-retained cells to be $\approx 10^{-15}$ A m^2 (Figure 2B). This value is above the estimate of the minimum magnetic moment of $\approx 10^{-16}$ A m^2 for a cell to be retained on a MACS column, assuming ≈1000 surface-bound commercial MACS beads.[32,33]

As for the iron content from internalized magnetic nanoparticles, Müller and colleagues found $\approx 1.1 \times 10^{-14}$ g_{Fe} derived from commercial MACS beads internalized in $CD133^+$ stem cells.[34] We can obtain a similar estimate of 1.65×10^{-14} g of ferrimagnetic iron per MACS-retained cell from the average magnetization in VSM and FMR (**Table 1**, see also the detailed calculation in the Supporting Information). The total amount of Fe per MACS-retained cell we measured by ICP MS is 8.9×10^{-13} g (cf. ICP MS data above) is almost two orders of magnitude more than in $CD133^+$ cells,[34] indicating that only a small fraction of the iron inside MACS-retained cells was ferrimagnetic, while the major fraction exhibited a paramagnetic response.

By VSM, we detected the magnetic hysteresis loop of MACS-separated cells with a total saturation magnetic moment ≈4 times higher than the detection limit, while three control samples had magnetic responses below the noise level (Figure 2). A standard zero-field cooled/field-cooled protocol in small external fields failed in these cases due to the low signal level. The temperature-dependent VSM measurement in high fields, however, reflected the presence of both ferrimagnetic and strong paramagnetic components in MACS-separated cells, in line with the evidence for ultrafine maghemite nanocrystallites dispersed in an amorphous matrix of a phosphorous-rich ferrihydrite-like phase in encapsulin cores (Figure 3).

Temperature- and angular-dependent FMR measurements were conducted to gain specific details about long-range magnetic ordering within encapsulin particles. This was anticipated to yield a combination of FMR signals and EPR from paramagnetic species within the sample. Distinguishing these contributions is straightforward because FMR is expected to exhibit uniaxial dependence of the resonance field after field-cooling, with a minimum in the field-cooling direction. This is due to the rotation of nanoparticles in the liquid state, aligning their easy axis with the field. In contrast, EPR lines remain unaffected by the direction of the external field.[35–37]

We detected an angular-dependent FMR line featuring uniaxial anisotropy, which we attribute to the ferrimagnetic component of the sample (Figure 2C).

As expected, the intensity of this line was only ≈5% of the main angular-independent EPR line, most probably corresponding to the paramagnetic matrix and biologically bound ferric iron. The observation of such uniaxial symmetry of the FMR line matches the above expectations for ferrimagnetic nanoparticles frozen in an external field from the liquid state. Therefore, we fitted FMR angular dependencies, assuming rod-like assemblies of encapsulin nanoparticles (or their preformed aggregates) formed in the liquid before subsequent freezing.[37] We further neglect crystalline anisotropy, which is motivated by FMR studies on individual bacterial magnetosome chains, in which the global uniaxial anisotropy of the chain outweighs the local crystalline anisotropy of the individual magnetite particles.[38,39] Under these rough estimates, the angular dependence of the FMR line solely depends on the magnetization of the encapsulin nanoparticles and their

uniaxial symmetry from field cooling (Figure 2 and Figure S3D, Supporting Information).

Independently of the VSM measurement, we extracted a (saturation) magnetization of 280 kA m^{-1} with the uncertainty of ±25% at T = 200 K by simulating the angular dependence with the magnetization of the ferrimagnetic component in the cells being the only fit parameter to describe the experiments (Figure S3E, Supporting Information). This result is important since it solely originates from the magnetization of the ferrimagnetic contribution of encapsulin nanoparticles producing the FMR line. Also, this estimate was used to normalize the VSM hysteresis loop of MACS-separated cells to the mass of ferrimagnetic Fe (as opposed to the total Fe mass in the cell pellet previously determined by the ICP MS). This way, we calculated the saturation magnetization M_s equal to 56.0 A m^2 kg^{-1}, consistent with magnetoferritin[19] or colloidal maghemite nanoparticles.[40] Importantly, our M_s value is higher than the value reported for the encapsulins from *M. xanthus* (15.3 A m^2 kg^{-1} at 10 kOe and 300K) filled with iron oxide under optimal in vitro conditions and exhibiting ferrimagnetic behavior.[41] In our case, the M_s only represents the characteristics of a minor fraction of the sample, which is mostly paramagnetic. Nonetheless, this property is remarkable since the magnetic material was produced by living mammalian cells under physiological conditions, not under in vitro conditions requiring high temperatures, alkaline pH, or the addition of external reducing agents, as in previous publications.[19,33,41]

Similar results were obtained from iron oxide cores of ferritin expressed in mesenchymal stem cells.[42,43] In Van de Walle et al.[42] M_s of ≈64.0 m^2 kg^{-1} was observed in the ferritin cores formed in stem cells after ≈10 days of incubation with pre-synthesized Fe_3O_4 particles. Recent research by Fromain et al.[43] exclusively utilized ferric quinate as the iron source in both human and mouse mesenchymal stem cells. Their findings indicated the formation of mixed ferrihydrite-maghemite particles within ferritin proteins following 14–36 days of continuous cell incubation in the iron-rich medium. This resulted in magnetic moments per cell of ≈2.0 × 10^{-15} A m^2, aligning with our results (Table 1) when normalized to the total intracellular Fe from ICP MS measurements. Additionally, they calculated the saturation magnetization of M_s ≈ 0.5–1.0 emu g^{-1} (= A m^2 kg^{-1}) normalized to the total iron content, encompassing both paramagnetic and long-range ordered ferrimagnetic Fe.[43] To differentiate the ferrimagnetic Fe from paramagnetic contributions, we conducted FMR measurements. Employing a simple model of rod-like magnetic nanoparticle structures after field-cooling, the sole fit parameter, sample magnetization, yielded M_s = 56.0 A m^2 per kg Fe. This value is comparable to the 64.0 A m^2 kg^{-1} observed after incubation with pre-synthesized Fe_3O_4 particles.[42]

With regard to the subcellular distribution of the iron-oxide-filled encapsulins in MACS-retained cells, our findings revealed that they agglomerated into large cytosolic aggregates exhibiting hexagonal close-packing of the protein shells and an iron core diameter of 31 ± 3 nm (Figure 3F), indicating a maximum loading of the ≈30 nm wide encapsulin lumen.[23] In the majority of cases, a discernible membrane surrounding the aggregate was not evident. Nevertheless, instances of encapsulin agglomerates with chain-like or rod-like morphology were also observed, which may indicate an association with the cytoskeleton. Furthermore, iron-oxide-filled encapsulins were also observed within endolysosomes and autophagosomes in MACS- and FACS-separated cells, as well as in non-sorted cells. This suggests the possibility of a process such as exocytosis, which may be responsible for eliminating excess encapsulins under these conditions of strong overexpression.

As previously established, the $QtEnc^{FLAG}$ structure contains multiple locations of QtIMEF, providing many sites for Fe oxidation and crystallization.[23,44] This may enable the simultaneous growth of the iron oxide core at multiple nucleation centers, leading to the absence of a well-defined crystalline structure.

By HAADF-STEM, we identified ultrafine crystallites of 1–3 nm in size that were embedded as "inclusions" of various orientations where local crystalline order does exist in the ≈30 nm-sized amorphous matrix of the encapsulin core. Although the dimensions of these inclusions were too small to determine the exact type of crystalline structure, their presence may indicate multiple iron oxide phases (Figure 4C).

According to EDX analysis, Fe, O, and P were the primary elemental constituents of the encapsulin nanoparticles. These had a Fe:P R_{at} of 1.1±0.2 in flow-through cells, similar to encapsulins from *Q. thermotolerans* expressed in *E. coli*[44] and bacterioferritins,[45,46] both of which have an approximate Fe:P R_{at} of 1.0. In distinction, the MACS-retained cells had a 20–30% higher average Fe:P R_{at} equal to 1.3±0.1 for dispersed encapsulins and 1.6±0.1 for aggregated encapsulins. Finally, in some instances, we observed a center-surround structure in encapsulin particles with a quasicrystalline Fe-rich center and a P-rich surround (Figure S6E, Supporting Information), which might be explained by the iron loading/release mechanism, similar to the one in ferritins, where the presence of phosphate facilitates iron release.[47] Phosphate could thus prevent the quasicrystalline iron-oxide phase within encapsulins from growing further. Such an inhibitive effect has long been known for ferritin cores, where the crystallinity of the nanoparticles formed inside the protein lumen is negatively influenced by the P stored inside,[48,49] while the overall quantity of phosphorus directly correlated with the phosphorus concentration in the medium of the cell culture.[50,51] The latter has been confirmed for the mammalian expression system where encapsulins in MACS-separated cells cultured in a low-phosphorus DMEM had a ≈20% higher Fe:P R_{at} (1.9±0.2) than MACS-separated cells cultured in a standard DMEM. Nonetheless, the iron oxide mineral in the encapsulin core of cells cultured in a low-phosphorus DMEM remained amorphous. In contrast, ferritins containing fully crystallized ferrihydrite in mammalian cells may display a Fe:P R_{at} of up to 10.0.[45,52] Therefore, scavenging strategies to further reduce the phosphorus content of encapsulins inside mammalian cells are of interest in the future.

Based on the XAS-STXM measurements, the major Fe species (71-85%) is a ferric iron oxide compound (Figure 5A,C). The small amount of ferrous iron (nominally of 15–29% FeO needed for a reasonable fit) may point to magnetite Fe_3O_4 in minor amounts. While FFT probes a long-range crystalline order (which is absent in our material), XAS allowed us to evaluate the local coordination of Fe atoms/Fe:O stoichiometry.

There are several ferric oxide/hydroxide candidate minerals consistent with our XAS spectra, particularly the polymorphs of Fe_2O_3 (hematite, maghemite), FeOOH (goethite, akaganeite, lepidocrocite, feroxyhyte), and ferrihydrite (disordered, ordered).

It is noteworthy that maghemite (γ-Fe_2O_3) and ordered ferrihydrite have an intrinsic ferrimagnetic lattice. Therefore, these two phases are the most consistent with our magnetic characterization results. Although the remaining minerals are nominally antiferromagnetic, they cannot be excluded based on XAS-STXM results alone, as they may exhibit defect-related ferrimagnetism when present as nanoparticles due to uncompensated spins. The latter, in particular, has been observed for akaganeite[53], but its Neel temperature is usually less than 300 K.[54] We verified these results by conducting a separate FMR/EPR measurement for the synthetic dextran-coated akaganeite particles at room temperature. This measurement revealed an FMR line at ≈125 mT and several EPR lines above 300 mT, proving the ferrimagnetic order (Figure S13, Supporting Information).

We also performed a complementary Raman microspectroscopy, which detects mineral-specific vibrational modes and thus allows differentiation among iron (hydr)oxide polymorphs in encapsulin cores. We deliberately chose to do the measurements in live cells to maximize the signal compared to the ultrathin cell cuts.

Raman microspectroscopy in live cells revealed a broad band at 700 cm^{-1}, consistent with maghemite γ-Fe_2O_3 and ferritin-derived ferrihydrite $[FeO(OH)]_8[FeO(H_2PO_4)]$ when measured on reference material using the same device under identical parameters.[28] These results align with those obtained from XAS/STXM, which confirms the absence of radiation damage in the latter analysis. The data also suggest that hematite (α-Fe_2O_3), a canted antiferromagnet with small net ferrimagnetism at room temperature, is either a minor constituent or not present in the aggregates of encapsulin particles in the MACS-separated cells since its peak at ≈613 cm^{-1} was not visible. Akaganeite (β-FeOOH) has a distinct Raman band at ≈720 cm^{-1},[29] which we did not detect in our MACS-retained cells. In our synthetic dextran-coated akaganeite sample (Figure S9B, Supporting Information), we identified the ≈720 cm^{-1} band in a form of a "shoulder" next to a strong band at ≈700 cm^{-1}, which may suggest some transformation to maghemite. A comparable "shoulder" was not clearly discernible in the MACS-retained cells, and a transformation to a maghemite-like phase is also possible in this case. Consequently, the presence of a minor fraction of akaganeite in the MACS-retained cells cannot be excluded.

Overall, several distinct peaks of hematite and akaganeite rather manifest themselves in the 135–415 cm^{-1} range, as evidenced by multiple spectra from natural and chemically synthesized hematite taken in the literature.[55]

Unfortunately, due to the strong Raman signals from the cytosolic proteins and other cell components, the peaks of magnetite, maghemite, hematite, ferrihydrite, akaganeite, or other iron-oxide/hydroxide phases in the range 50–600 cm^{-1} or 750–1200 cm^{-1} were not accessible for evaluation.[30,56–60]

Therefore, we arrived at the following conclusions from the combination of our complementary analytical techniques: first, hematite α-Fe_2O_3 is not consistent with a main phase in the encapsulin lumen based on our magnetic characterization and Raman microspectroscopy. Second, the presence of magnetite Fe_3O_4 is unlikely based on the XAS and Raman spectra. Third, ordered ferrihydrite $[FeO(OH)]_8[FeO(H_2PO_4)]$ is possible as a main constituent from the magnetic and Raman/XAS characterization, but it is less likely since it only precipitates after several hours of heating at a high temperature. Additionally, akaganeite β-FeOOH, which can possess uncompensated, ferrimagnetically coupled surface spins, can contribute to the ferrimagnetic signal from the MACS-retained cells, and the presence of akaganeite cannot be ruled out from our intracellular Raman microspectroscopy. Consequently, the iron (III) oxide phase that most likely explains the ferrimagnetic behaviour observed in the VSM/FMR measurement as a main constituent, consistent with the results of all analytical techniques we used, is maghemite γ-Fe_2O_3.

We also demonstrated the magnetic manipulability of MACS-separated cells by positioning a magnetic needle under the control of a fluorescent microscope. The tip of this needle produced an estimated magnetic gradient of ≈5×10^3 T m^{-1} at 10 µm distance (Figure S10, Supporting Information). It should be kept in mind that this experiment was carried out in a droplet of cells suspended in DPBS, so the majority of cells was not visible in the focal plane. A thorough examination of the Video S1A,B, Supporting Information, pertaining to the MACS-separated cells in DPBS, reveals that solely cells traversing the tip at a relatively low velocity (Brownian motion) are captured by the magnetic tip, while cells exhibiting higher velocity are largely unperturbed. This phenomenon can be elucidated by calculating the magnetic force on the cells. The mean magnetic moment per MACS-separated cell was determined to be 10^{15} A m^{-2} (see Section 2.3). The total magnetic moment of the ferrimagnetic encapsulins within a cell, when multiplied by the gradient field (see Figure S10, Supporting Information), yields the magnetic force exerted on the cell.[12,61] For simplicity, we restrict ourselves to the largest gradients along the tip direction (Figure S10D, Supporting Information). The attractive force at the tip in y-direction is 29 pN at the tip and decays to only ≈5 pN at a distance of 50 µm. These are typical forces for successfully capturing magnetically labeled cells in similar experiments using needles.[62] The Video S1A,B, Supporting Information, shows that the cells are captured from a conical zone (narrower near the tip and widening with distance from it) with maximum dimensions of 50–100 µm in y-direction and ~2x shorter maximum width in x-direction. The data, however, does not allow for a statistical analysis. Similar observations with a comparable magnetic field gradient were previously reported for magnetite-loaded ferritins, which were, however, produced under optimal in vitro conditions[19,33,63] or upon the intracellular degradation of chemically synthesized Fe_3O_4 nanoparticles.[42]

4. Conclusion

While previous studies on genetically controlling biomagnetism have worked with bacteria[64] and yeast,[16] we focused on mammalian cells, overexpressing iron-biomineralizing bacterial encapsulin nanocompartments. We found that after transient co-expression of the encapsulin shell and ferroxidases from *Q. thermotolerans* together with an iron importer in the presence of iron ammonium sulfate for a few days, a small fraction of these cells can be retained on commercial MACS columns and show agglomerates of densely packed iron-oxide cores that contained nanocrystalline inclusions inside an amorphous iron-oxide matrix leading to the mixed para- and ferrimagnetic behavior.

The resulting total magnetic moment of ≈10^{-15} A m^2 enabled cell manipulation via magnetic gradients around a magnetic

needle or bulk permanent magnets, causing patterned HEK293T cell growth.

We conclude that the most parsimonious explanation for the ferri- and paramagnetism measured from the MACS-retained cells obtained from our data from cellular imaging, ultrastructural, elemental, local electronic, and chemical structure analyses is that the iron-oxide encapsulin cores are composed of a quasicrystalline maghemite phase embedded within an amorphous iron-oxide-phosphorous matrix.

Our comprehensive analytical pipeline provides the foundation for future bioengineering efforts to systematically improve the magnetic properties of encapsulins. As the genetically expressed encapsulins are directly available in the cytosol and do not require delivery to the cells, which often results in lysosomal entrapment, they may eventually permit magnetic manipulation of molecular processes in living mammalian cells under genetic control.

5. Experimental Section

Genetic Constructs: Mammalian codon-optimized QtEnc (UniProt: A0A0F5HPP7_9BACI) and QtIMEF *from Q. thermotolerans* (UniProt: A0A0F5HNH9_9BACI) were custom synthesized by Integrated DNA Technologies and cloned into pcDNA3.1 (+) Zeocin (Invitrogen) using restriction cloning or Gibson assembly. C-terminally FLAG-tagged *Mus musculus* Zip14^{FLAG} (UniProt: Q75N73) was inserted into pcDNA 3.1 (+) Zeocin via restriction cloning. A FLAG epitope tag was C-terminally appended to QtEnc for expression in HEK293T cells using Q5 Site-Directed Mutagenesis (New England Biolabs). Multigene expression of QtIMEF, QtEnc^{FLAG}, and mScarlet-I (https://www.addgene.org/104007/) was achieved by generating a genetic cassette containing QtIMEF and QtEnc^{FLAG} separated by a P2A peptide. Then, QtIMEF-P2A-QtEnc^{FLAG} was cloned upstream of an ECMV internal ribosome entry site (IRES2, denoted as IRES in the main text and figure), whereas mScarlet-I was inserted downstream, yielding a single QtIMEF-P2A-QtEnc^{FLAG}-IRES2-mScarlet-I construct. To target mEos4b as cargo to the QtEnc^{FLAG} nanocompartments, the fluorescent protein was C-terminally fused to a 2 × GGGGS linker followed by the minimal encapsulation signal LTVGSLRR (QtSig). To generate the destabilized version of mEos4b, the L106P mutant of FKBP12 (DD-N,[65] was N-terminally appended to mEos4b-EncSig using Gibson-Assembly yielding DD-mEos4b-QtSig. For a complete list of the genetic constructs featuring their composition, refer to Table S1, Supporting Information.

Cell Culture and Protein Expression: Low passage number HEK293T (ECACC: 12 022 001) cells were cultured in the advanced DMEM (Gibco) with 10% fetal bovine serum (FBS, Gibco) and Penicillin-Streptomycin (Gibco) at 100 µg mL^{-1} (will be further referred to as a complete DMEM) at 37 °C and 5% CO_2. Cells were transfected with X-tremeGENE HP (Roche) according to the protocol of the manufacturer. DNA amounts (ratio shell to cargo) were kept constant in all transient experiments to yield reproducible DNA-Lipoplex formation. To express combinations of QtEnc^{FLAG} with cargo proteins and a low-level Zip14^{FLAG} co-expression (or, in case of control experiments, with DD-mEos4b-QtSig replacing QtIMEF and eYFP replacing Zip14^{FLAG}), 65% of the total DNA amount encoded the shell, 30% of the total DNA were used for the respective cargo, and the remaining 5% encoded Zip14^{FLAG} (or eYFP). For the transfection with a QtIMEF-P2A-QtEnc^{FLAG}-IRES2-mScarlet-I plasmid (or QtIMEF-P2A-QtEnc^{FLAG}-IRES2 plasmid for Raman microspectroscopy), 95% of the total DNA encoded shell and cargo while 5% encoded Zip14^{FLAG}. In the case of the control transfection with IRES2-mScarlet-I plasmid ("no encapsulins" condition), 100% of the total DNA encoded this plasmid.

To facilitate iron loading, cells were supplemented with medium containing ferrous ammonium sulfate (FAS) at indicated concentrations 24 h after transfection. For analysis of protein expression, cells were harvested 48 h after the FAS supplementation and lysed with M-PER Mammalian Protein Extraction Reagent (Pierce Biotechnology) containing a mammalian protease inhibitor cocktail (SIGMA P8340, Sigma-Aldrich) according to the protocol of the manufacturer. After spinning down cell debris at 10 000 x g for 15 min, cell lysates were kept at 4 °C for downstream analyses. Protein concentrations of the lysates were determined by measuring OD at 280 nm.

Blue Native Gel Electrophoresis and On-Gel Analyses: To detect native encapsulins, pre-cast NativePAGE Novex 3–12% Bis-Tris gels (Life Technologies) were used according to the manufacturer's protocol. Gels were loaded with whole cell lysates (obtained with an M-PER reagent, cf. above), mixed with NativePAGE Novex sample buffer, and run for 120 min at 150 V. Unstained Protein Standard (Life Technologies) covering a size range between 20 – 1200 kDa was used as a marker. The total protein amount of whole cell lysates loaded per well was adjusted to ≈1 µg. Gels loaded with whole-cell lysates were Coomassie-stained using Bio-Safe Coomassie Stain (Bio-Rad Laboratories). For the detection of iron-containing proteins, gels were Prussian Blue (PB) stained. Briefly, gels were incubated in 2% potassium hexacyanoferrate (II) in 10% HCl for 45 min. For 3,3′-Diaminobenzidine (DAB)- enhancement (DAB PB), gels were washed three times with ddH_2O and incubated in 0.1 M phosphate buffer pH 7.4 containing 0.025% DAB and 0.005% H_2O_2 until dark-brown bands appeared. Gels were washed three times with ddH2O to stop DAB polymerization.

Quantification of Cellular Iron Content: To quantify the iron content in HEK293T cell pellets, inductively coupled plasma-mass spectrometry (ICP-MS) was performed. Measurements were performed on a NexION 350D (Perkin Elmer) in collision mode with kinetic energy discrimination (KED). Cell pellets (8×10^6 cells each) were dissolved in 50 µL of 70% nitric acid for 2 h at 65 °C, then incubated at room temperature overnight and diluted 1:10 with deionized water.

Magnetic-Activated Cell Sorting: Low passage number HEK293T cells were cultured in 6-well plates and transfected with one of the following DNA mixtures (% of the total DNA):

- QtIMEF-P2A-QtEnc^{FLAG}-IRES2-mScarlet-I (95%) and Zip14^{FLAG} (5%);
- QtIMEF-P2A-QtEnc^{FLAG}-IRES2 (95%) and Zip14^{FLAG} (5%);
- QtEnc^{FLAG} (65%), DD-mEos4b-QtSig (30%), and Zip14^{FLAG} (5%);
- QtEnc^{FLAG} (65%), DD-mEos4b-QtSig (30%), and eYFP (5%);
- IRES2-mScarlet-I (100%);

24 h post-transfection, cells were supplemented with 2 mM FAS. 48 h after the addition of FAS, cells were washed with 1xDPBS (500 µL per well) twice, detached with Accutase (Sigma-Aldrich, 10 min at 37 °C, 1 mL per well), and centrifuged at 500 RCF for 4 min at RT. Before sorting, cell pellets were resuspended in 500 µL of 1xDPBS supplemented with 2% FBS. For magnetic sorting, columns filled with ferromagnetic spheres (MS columns, Miltenyi Biotec) were placed in an external magnetic field (OctoMACS separator, Miltenyi Biotec) and equilibrated with 500 µL of 1xDPBS supplemented with 2% FBS. The column was loaded with cells and washed with 500 µL of 1xDPBS supplemented with 2% FBS twice; the flow-through was collected as one fraction. After removing the column from the magnetic separator, cells were eluted with 500 µL of 1xDPBS supplemented with 2% FBS. The total numbers of MACS-separated cells, flow-through cells, non-sorted cells, and control cells ("no encapsulins" condition) were determined by manual counting in Neubauer Improved DHC-N01 chambers.

Fluorescence-Activated Cell Sorting: FACS was performed on the BD FACSaria II system (controlled with the BD FACSDiva Software, v.6.1.3, BD Biosciences). HEK293T cells were either co-transfected with QtIMEF-P2A-QtEnc^{FLAG}-IRES2-mScarlet-I (95% of the total DNA) and Zip14^{FLAG} (5% of the total DNA) or co-transfected with QtIMEF-P2A-QtEnc^{FLAG}-IRES2 (95% of the total DNA) and Zip14^{FLAG} (5% of the total DNA) in 6-well plates (cf. above) and supplemented with 2 mM FAS 24 hours post-transfection. 48 hours after the addition of FAS, adherent cells were washed with 1xDPBS (500 µL per well) twice, detached with Accutase (Sigma-Aldrich, 10 min at 37 °C, 1 mL per well), and centrifuged at 500 RCF for 4 min at RT. Cell pellets were resuspended in 500 µL of 1xDPBS supplemented with 2% FBS, transferred into conical 5 mL polystyrene round-bottom tubes, including a cell-strainer cap, and kept on ice. The main cell population was first gated

according to forward scatter and sideward scatter (Gate P1, Figure S4, Supporting Information). Next, single cells were chosen according to their FSC-A and FSC-W values (Gate P2). Subsequently, the transfected cells were gated according to their red fluorescence (610 nm) due to mScarlet-I expression. The fraction isolated via Gate P3 contained the 2% of cells with the strongest mScarlet-I fluorescence, while Gate P6 was chosen to isolate the cells with the weakest mScarlet-I fluorescence.

Cell Viability Assays: Iron-related cytotoxicity associated with the loss of cellular membrane integrity was monitored via the LDH-Glo Cytotoxicity Assay (Promega) according to the manufacturer's protocol in the whole population of cells co-transfected with QtIMEF-P2A-QtEnc^{FLAG}-IRES2-mScarlet-I (95% of the total DNA) and Zip14^{FLAG} (5% of the total DNA) and cultured in the complete DMEM supplemented with FAS in 0–2.0 mM concentration range for 48 h. The cell viability assay was performed in a 96-well plate format as an endpoint measurement. Luminescence readings were taken on a Centro LB 960 (Berthold Technologies, Bad Wildbad, Germany) at 0.5 s acquisition time. The viability of cells supplemented with 0 mM FAS was taken as 100%; the viability of non-transfected HEK293T cells treated with 0.2% Triton X-100 was taken as 0%. Cell viability after replating was evaluated in MACS-separated cells and flow-through cells immediately after the MACS procedure using non-sorted cells as a control. The cells were resuspended in a complete DMEM (1×10^5 cells mL^{-1}) and seeded in wells of a 12-well plate. 24 h later, the cells were stained either with DAPI (MACS-separated, flow-through, and control cells) or Hoechst 33 342 (MACS-separated cells) dyes according to the protocol of the manufacturer (Sigma-Aldrich). Briefly, the cells were washed with 1xDPBS twice, and either 0.1 µg mL^{-1} of DAPI or 1 µg mL^{-1} of Hoechst 33 342 (both suspended in 1xDPBS) was added to the cells for 5 min. Afterward, the cells were washed with 1xDPBS twice and imaged in an EVOS fluorescence microscopy system (Invitrogen). Bright-field phase microscopy images and fluorescence microscopy images in the DAPI channel (DAPI/Hoechst signal) and in the RFP channel (mScarlet-I signal) were acquired. In a control experiment, non-sorted cells were first treated with either 50 µM digitonin (positive control) or 1xDPBS (negative control) for 10 mins, then washed with 1xDPBS twice and stained according to the same protocol as described above. DAPI is known to only inefficiently pass through intact cell membranes and, therefore, preferentially stains the nuclei in dead cells,[66] while Hoechst 33 342 stains both live and dead cells. Thus, the absence of the DAPI signal and the presence of the Hoechst signal indicate that the cell membrane integrity is likely not compromised.

Magnetic Manipulation (Experiment with a Magnetic Needle): A needle made of Permalloy-80 (ESPI metals, USA) attached to a custom-made permalloy cone and a permanent NdFeB magnet (Supermagnete, Germany) was mounted on a micromanipulator device (Narishige, USA). Magnetic field gradients near the needle tip were simulated using Finite Element Method Magnetics (FEMM) 4.2 software (https://www.femm.info/). Immediately after the MACS procedure, MACS-separated cells, flow-through cells, non-sorted cells, and control ("no encapsulins") cells were resuspended in 1xDPBS supplemented with 2% FBS (1×10^5 cells mL^{-1}) and transferred to Ibidi 35 mm μ-Dish (ibiTreat, Low; Ibidi, USA). The cells were imaged in an RFP channel (due to the presence of mScarlet-I in the DNA construct) of Zeiss Axioplan 2 fluorescence microscope with an Olympus UMPLFLN 10XW water immersion objective. As soon as the needle was immersed in the cell suspension, a sequence of images taken every 1s was recorded with Ximea PCIe x4 Gen2 camera using Ximea CamTool software.

Image Analysis – Magnetic Manipulation: A sequence of images from the magnetic manipulation of cells with the needle was recorded within the first 5 minutes after the immersion of the needle in the corresponding cell suspensions. Fluorescence imaging movies were low-pass filtered along the temporal dimension in MATLAB using a custom-built IIR filter and the filtfilt function. Filtering allowed to keep low-frequency components, i.e., cells adhering to the needle intact, while removing high-frequency components, i.e., out-of-focus floating cells. A baseline fluorescence level was calculated from the first ten imaging frames, and the percentage change relative to this baseline was computed on a per-pixel basis. Subsequently, the normalized fluorescence intensity in the RFP channel from a triangular-shaped ≈30 000 µm^2 area of the image at the needle tip was extracted and used for further quantification.

Magnetic Manipulation (Patterned Cell Growth): Immediately after the MACS procedure, MACS-separated cells, flow-through cells, and no encapsulin cells were resuspended in a complete DMEM (1×10^5 cells mL^{-1}) and seeded in a well of a 12-well plate with either neodymium-50 magnetic or aluminum cube (Supermagnete, Germany) of 5 mm size in each dimension. 24 h after replating, bright-field phase microscopy images and fluorescence microscopy images in the RFP channel (due to the presence of mScarlet-I in the DNA construct) were acquired using an EVOS fluorescence microscopy system (Invitrogen).

TEM Sample Preparation: For the TEM sample preparation, the standard staining method was adapted.[67] HEK293T cells were collected with Accutase (Sigma-Aldrich) immediately after the sorting procedure in case of MACS/FACS-separated cells or 48 h after FAS supplementation in case of the non-sorted cells and cells transfected with a plasmid encoding mScarlet-I protein and IRES2 ("no encapsulins" condition). The cells were spun down at 1000 RCF for 3 min at room temperature (RT). The material was fixed by the addition of 2,5% glutaraldehyde (Electron Microscopy Sciences) in 0.1 M sodium cacodylate buffer (pH 7.4, Electron Microscopy Sciences) for 1 h at RT. After removal of the fixative, the cell pellet was supplemented with 200 µL of low-melting agarose (4%) in 0.1 M sodium cacodylate buffer, then the cells were spun down at 1000 RCF for 3 min at RT and left on ice for 20 min. The samples were postfixed with 1% osmium tetroxide solution (Electron Microscopy Sciences) and incubated for 1 h at 4 °C. The post-fixative solution was removed, and the material was washed three times with 0.1 M sodium cacodylate buffer at 4 °C. The buffer was removed, and the sample was subjected to dehydration by following increasing ethanol concentrations (at each concentration, the incubation step lasted for 15 min): 30%, 50%, 70%, 96%, 100% (twice), before proceeding to epoxy embedding. The epoxy medium for the embedding process was prepared as follows: 61.5 g 2-dodecenylsuccinic-acid anhydride (Serva) was mixed with 81.5 g of methyl nadic anhydride (Serva) as well as with 130.5 g glycidether 100 (Serva). The resulting mixture was stirred, and 3.750 µL of 2,4,6-tris(dimethylaminomethyl)phenol (Serva) was added to the mixture, stirred, and aliquoted for storage at −20 °C. Immediately after the last washing step, the sample was subsequently immersed in the following mixtures (all steps at RT for 30 min): ethanol: resin (3:1), ethanol: resin (1:1), ethanol: resin (3:1). Finally, the sample was immersed in the pure resin for 30 min at RT, then re-immersed in another portion of resin and left overnight. Afterward, the sample was transferred to the bottom of the pyramid tip-shaped rubber mold and cured at 60 °C for 72 h for the resin polymerization. The resulting blocks were subjected to trimming and slicing. The trimming of excess epoxy from the block's surface was done using an EM TRIM milling system (Leica Microsystems). Using an UltraCut E microtome (Reichert/Leica), the prepared blocks were prepared with a histo-knife (DIATOME) and then sequentially cut with an ultra-knife (DIATOME) at a slice thickness of 70 nm, verified by the slices' interference pattern. The slices were deposited on the surface of 200 mesh copper grids (Plano) and postcontrasted using 0.5% uranyl acetate (Electron Microscopy Sciences) for 30 min and Ultrostain2 for 1.5 min (3% lead citrate, Leica).

TEM Images Acquisition: TEM images were acquired on a Libra120 TEM (Carl Zeiss GmbH), equipped with a CCD camera (TRÖNDLE Restlichtverstärkersysteme) using ImageSP software (SYSPROG). Before image acquisition, all grid-supported specimens were pre-irradiated at 120 kV beam voltage and 200 µrad illumination angle without apertures. The actual image acquisition was done with the activated BIO-AIS condenser aperture system and a 60 µm objective aperture. The same beam conditions used for pre-irradiation were also applied for imaging, except for an illumination angle of 100 µrad.

Image Segmentation Analysis: TEM images of MACS-retained, flow-through, or FACS-retained cells (92 images for MACS-retained cells, 90 images for the flow-through and FACS-retained cells) were segmented using Biodock (Biodock, AI Software Platform. Biodock 2024. Available from https://www.biodock.ai) to generate annotations for iron oxide nanoparticles and cell areas. The spatial distribution of segmented iron oxide cores was analyzed using the OPTICS algorithm[68] to obtain density-based

clusters. Segmented iron-oxide cores were hierarchically ordered according to their "reachability distance," and clusters were defined such that a minimum of 50 particles (parameter min_samples) were found within a radius of 370 pixels (parameter eps). Thereby, iron oxide nanoparticles were categorized as aggregated or dispersed, allowing the calculation of aggregate area for each individual aggregate by drawing alpha shapes. Additionally, higher resolution TEM images of MACS-retained cells showing dense, hexagonal close-packaged iron oxide nanoparticles (6 images) were segmented in Biodock (Biodock, AI Software Platform. Biodock 2024. Available from https://www.biodock.ai) to obtain annotations for iron oxide nanoparticles and empty shells. The diameter of iron oxide nanoparticles and empty shells was determined from the area-equivalent diameter. To assess the inter-particle distance, the annotations were filtered for nanoparticles and shells with six neighbors, and the inter-particle distance was calculated using the k-nearest neighbor algorithm.[68]

High-Angle Annular Dark-Field Imaging in the Scanning Transmission Electron Microscopy Mode and Energy-Dispersive X-Ray Spectroscopy: HAADF-STEM images and EDX maps/spectra were obtained using a Titan Themis Z transmission electron microscope equipped with a DCOR+ spherical aberration corrector and a system of 4 super wide-angle Super-X X-ray detectors. The accelerating voltage of the source was 200 kV. The samples were prepared according to the same protocol previously used for the examination by a standard TEM. Image acquisition and analyses were conducted between November 2020 and November 2021.

X-Ray Absorption Spectroscopy in the Synchrotron Radiation-Assisted Scanning Transmission X-Ray Microscopy: Soft X-ray absorption is a technique that uses a brilliant, tunable source of X-rays with energies between 200 and 2000 eV, or wavelengths between 0.5 and 5 nm. X-ray absorption in this range is element-specific and sensitive to the chemical, electronic, and magnetic state of a sample. In scanning transmission X-ray microscopy, the sample is scanned through a focused X-ray beam, while the transmitted intensity is detected with a photodiode.[69,70] The excitation of 2p electrons into 3d valence states is directly affected by the symmetry and the neighbors of the atomic species that is probed, which is why it is possible to differentiate between, e.g., different iron oxides.[71] The STXM experiments described in this paper were performed at beamline 11.0.2.2 at the Advanced Light Source user facility at Lawrence Berkeley National Laboratory. Beamline 11.0.2.2 is an elliptical undulator beamline with full polarization control between 200 and 2000 eV.[72] The measurements were performed using a zone plate with a 25 nm outer zone width, providing a spatial resolution of ≈30 nm. Single images were acquired with a step size of 10 to 20 nm and exposure time per pixel between 1 and 5 ms. The spectra were obtained from images taken at different photon energies with 20 nm step size and 50 ms exposure per pixel. All X-ray absorption spectra, including the references, were acquired at the same beamline. Reference spectra used for fitting were normalized on a per-atom basis. X-ray absorption spectra of Fe_2O_3, FeO, Fe_3O_4, and $FePO_4$ were previously reported.[27] Ferritin from equine spleen (Sigma-Aldrich) was used to obtain the reference spectrum of ferritin.

Raman Microspectroscopy: Raman spectra of MACS-retained cells containing encapsulin particles were collected using a Lab-RAM HR Raman microscope (Horiba Scientific, France) with an integrated Olympus BXFM microscope. The measurements were performed with a 633 nm diode laser (max. 9 mW at the sample). Wavelength calibration was accomplished by the characteristic first-order phonon band of Si at 520.7 cm^{-1}. For the experiment, MACS-separated cells previously transfected with QtIMEF-P2A-QtEnc^{FLAG}-IRES2 (cf. detailed description in "Cell culture and protein expression" section) were resuspended in a complete DMEM (1×10^5 cells mL^{-1}) and replated on a round glass coverslip (#1.5, 18 mm diameter) coated with poly-L-lysine. 24 h later, cells were carefully washed with 1xDPBS, and the coverslips were placed in a well of a 6-well plate filled with sterile 1xDPBS for the measurement. The laser beam was focused onto the sample with a 60× water immersion objective (Olympus MPlan N, NA = 0.9). The acquisition time for one spectrum was set to 10 s, and 25 repetitions were chosen to obtain a reasonable signal-to-noise ratio. Typical Raman bands for phenylalanine appear at 1002 cm^{-1}, regarded as protein markers.[73]

Raman spectra of the reference sample of dextran-coated akaganeite particles (https://www.sigmaaldrich.com/DE/de/product/sigma/d8517) were obtained using a WiTec alpha300RAS System. The measurements were performed with a 532 nm laser (0.505 mW at the sample). For the measurements, the slide was coated with a gold film (to suppress the Raman line of glass), and a drop of dextran-coated akaganeite solution was placed on the slide. The laser beam was focused onto the sample with a 20× objective (Zeiss EC Epiplan, NA = 0.4). The acquisition time for one spectrum was set to 0.5 s, and 500 repetitions were chosen to obtain a reasonable signal-to-noise ratio.

Vibrating Sample Magnetometry: The field-dependent magnetization of all samples was measured at various temperatures from 3 to 200 K and B = ± 9T in a Quantum Design PPMS DynaCool system. Cell pellets of all samples were collected by a pipette with enhanced tip diameter and transferred into synthetic capsules. The number of cells was measured independently by manual counting. The total amount of Fe in the capsule of the sorted cells was determined after VSM by ICP-MS. All samples were frozen in a zero field before measurements were performed to avoid any movement of encapsulin particles in external magnetic fields or sample spilling. The magnetic response of the samples is highly dominated by the organic material's and water's diamagnetism for temperatures above 15 K. Below, Langevin-type paramagnetic contribution becomes dominant, which is the sum of all paramagnetic ions in the sample. To separate diamagnetic, paramagnetic, and ferrimagnetic contributions, we assume temperature-independent diamagnetism, paramagnetic signals obeying the Curie law (likely from different origins), and a residual ferrimagnetic signal. The raw magnetic high-field susceptibility χ_{HF} is calculated and multiplied by temperature. The resulting linear slope is subtracted, removing the diamagnetic part. After this, the paramagnetic and ferrimagnetic contributions can be separated for temperatures above 50 K, assuming a linear response of the paramagnet.

Ferromagnetic/Electronic Paramagnetic Resonance: X-Band FMR/EPR of the MACS-separated cells (batch 1) has been measured in the same capsule used for VSM in a Bruker Elexsys E-500 system. The sample has been cooled in a helium cryostat to $T = 50$ K in B = 1T, defining the starting angle $\Phi = 0°$ for the angular-dependent FMR spectra at a frequency of 9.412 GHz at $T = 50$ K and $T = 200$ K.

FMR/EPR of the reference sample of the dried dextran-coated akaganeite particles (https://www.sigmaaldrich.com/DE/de/product/sigma/d8517) were measured on a Bruker Elexsys E-500 system from 1.2 to 0 T field with the following parameters: 15 G modulation, 54 dB gain, 80 ms time constant, 8192 points per measurement, 10 dB microwave power. Q empty cavity: 8600; Q (sample in the EPR quartz tube): 1200.

Statistical Analysis: Unpaired t-tests, Mann-Whitney tests, or Kruskal-Wallis tests with Dunn's multiple comparisons were performed using GraphPad Prism 10 (GraphPad Software, San Diego, California, USA). All error bars given are average values ± standard deviation (SD). A detailed table of all statistical analyses is given in Table S6, Supporting Information.

Supporting Information

Supporting Information is available from the Wiley Online Library or from the author.

Acknowledgements

The authors acknowledge Anja Ammer for assisting with the TEM sample preparation and MACS experiments, Stefanie Winkler for assisting with the TEM sample preparation, Susanne Pettinger for advising on the on-gel analyses, ICP MS, and MACS experiments, Ejona Rusha, Dr. Dong-Jiunn Jeffery Truong, and Niklas Armbrust for advising on the FACS experiment, Zoe Bousraou for assisting with the FACS experiment and advising on the magnetic manipulation experiment, PD Dr.-Ing. habil. Bernhard Gleich for providing permalloy cones for the magnetic manipulation experiment, and

Christine Benning for assisting with the ICP MS data acquisition. This research used resources of the Advanced Light Source, a U.S. DOE Office of Science User Facility under contract no. DE-AC02-05CH11231.

This research was funded by Helmholtz-RSF Joint Research Groups funding program number HRSF-0064 and RSF grant number 19-45-06302. M.V.E. gratefully acknowledges the support of the Humboldt Research Fellowship for Postdoctoral Researchers provided by the Alexander von Humboldt Foundation, the support from the Federation of European Biochemical Societies (FEBS) via a Long-Term Fellowship, the support of the Add-on Fellowship for Interdisciplinary Life Science provided by the Joachim Herz Foundation, and the funding from the European Union's Horizon 2020 research and innovation programme under the Marie Skłodowska-Curie grant agreement no. 899 987. G.G.W. acknowledges support from the European Research Council under grant agreements ERC-StG 311552 and ERC-COG 865710. The authors also acknowledge the financial support of the German Science Foundation (DFG) in the framework of the Collaborative Research Centres, Transregio 270 (CRC-TRR 270, Project No. 405 553 726 to U.W. and M.F.), CRC 1372 (project No. 395 940 726 to M.W.), and DFG INST 184/222-1 (M.W.). European Research Council, ERC-StG 311552, ERC-COG 86571, Humboldt Research Fellowship for Postdoctoral Researchers by the Alexander von Humboldt Foundation, Federation of European Biochemical Societies (FEBS) via a Long-Term Fellowship, Add-on Fellowship for Interdisciplinary Life Science by the Joachim Herz Foundation, European Union's Horizon 2020 research and innovation programme under the Marie Skł;odowska-Curie grant agreement no. 899987, German Science Foundation (DFG) in the framework of the Collaborative Research Centres, Transregio 270 (CRC-TRR 270): 405553726, German Science Foundation (DFG) in the framework of the Collaborative Research Centres, CRC 1372: 395940726, German Science Foundation (DFG): INST 184/222-1, RSF grant number: 19-45-06302.

Open access funding enabled and organized by Projekt DEAL.

Conflict of Interest

The authors declare no conflict of interest.

Author Contributions

M.V.E. conceptualized the study, designed the experiments, conducted and analyzed data from experiments in cell culture, on-gel analyses, ICP MS, MACS, FACS, TEM, and magnetic manipulation experiments, interpreted the data, wrote the manuscript, and secured funding, U.W. conducted VSM experiments, analyzed and interpreted VSM and FMR data, advised on the design of XAS/STXM and magnetic manipulation experiments, and wrote the manuscript, F.S. generated the expression constructs and advised on the design of experiments in cell culture, MACS, magnetic manipulation experiments, ICP MS, and on-gel analyses, S.B. co-conducted and analyzed data from the magnetic manipulation experiment, H.O. acquired, analyzed and interpreted XAS/STXM data, T.F. analyzed and interpreted XAS/STXM data, R.M. acquired and analyzed FMR data, L.P. segmented TEM data for the quantification of the agglomeration state of the iron-oxide cores, J.F. measured and modeled the magnetic field of the magnetic needle, I.B. acquired and analyzed the Raman microspectroscopy data, N.I. analyzed and interpreted the Raman microspectroscopy data, I.B.A. co-analyzed and interpreted the TEM data and advised on the TEM data acquisition, A.S.G. co-analyzed and interpreted the TEM data, A.S.S co-conducted cell-culture experiments and MACS experiments, F.C. performed Raman spectroscopy of the reference sample of akaganeite particles, N.J. performed the FMR/EPR measurement of the reference sample of akaganeite particles, S.W. interpreted the XAS/STXM data, M.F. interpreted the TEM data and advised on the design of the VSM/FMR experiments, R.L. interpreted data from the magnetic manipulation experiment and secured funding, M.A.A. acquired HAADF-STEM/EDX data and secured funding, M.W. advised on the VSM, FMR, and XAS/STXM experiments and the data interpretation, G.G.W. initiated and conceptualized the study, designed the experiments, wrote the manuscript, secured funding, and supervised the research.

Data Availability Statement

The data that support the findings of this study are available from the corresponding author upon reasonable request.

Keywords

encapsulins, genetically encoded magnetic nanoparticles, iron oxide biomineralization, magnetic-activated cell sorting, MACS, magnetomechanical cell manipulation, mammalian cells, structural and magnetic characterization

Received: September 24, 2024
Revised: December 21, 2024
Published online: January 16, 2025

[1] H. Huang, S. Delikanli, H. Zeng, D. M. Ferkey, A. Pralle, *Nat. Nanotechnol.* **2010**, *5*, 602.
[2] R. J. Mannix, S. Kumar, F. Cassiola, M. Montoya-Zavala, E. Feinstein, M. Prentiss, D. E. Ingber, *Nat. Nanotechnol.* **2007**, *3*, 36.
[3] R. B. Frankel, R. P. Blakemore, R. S. Wolfe, *Science* **1979**, *203*, 1355.
[4] D. Faivre, D. Schüler, *Chem. Rev.* **2008**, *108*, 4875.
[5] M. Pósfai, C. T. Lefèvre, D. Trubitsyn, D. A. Bazylinski, R. B. Frankel, *Front. Microbiol.* **2013**, *4*, 344.
[6] H. A. Lowenstam, *Science* **1967**, *156*, 1373.
[7] L. M. Gordon, D. Joester, *Nature* **2011**, *469*, 194.
[8] M. Dumont, T. Tütken, A. Kostka, M. J. Duarte, S. Borodin, *J. Struct. Biol.* **2014**, *186*, 38.
[9] M. R. Bellinger, J. Wei, U. Hartmann, H. Cadiou, M. Winklhofer, M. A. Banks, *Proc. Natl. Acad. Sci. USA* **2022**, *119*, e2108655119.
[10] T. Kim, D. Moore, M. Fussenegger, *J. Biotechnol.* **2012**, *162*, 237.
[11] S. A. Stanley, L. Kelly, K. N. Latcha, S. F. Schmidt, X. Yu, A. R. Nectow, J. Sauer, J. P. Dyke, J. S. Dordick, J. M. Friedman, *Nature* **2016**, *531*, 647.
[12] M. Meister, *elife* **2016**, *5*, e17210.
[13] P. Anikeeva, A. Jasanoff, *eLife* **2016**, *5*, e19569.
[14] S. Nimpf, D. A. Keays, *EMBO J.* **2017**, *36*, 1643.
[15] D. He, J. Marles-Wright, *N. Biotechnol.* **2015**, *32*, 651.
[16] Y. Matsumoto, R. Chen, P. Anikeeva, A. Jasanoff, *Nat. Commun.* **2015**, *6*, 8721.
[17] X. Liu, P. A. Lopez, T. W. Giessen, M. Giles, J. C. Way, P. A. Silver, *Sci. Rep.* **2016**, *6*, 38019.
[18] T. L. Li, Z. Wang, H. You, Q. Ong, V. J. Varanasi, M. Dong, B. Lu, S. P. Paşca, B. Cui, *Nano Lett.* **2019**, *19*, 6955.
[19] D. Liße, C. Monzel, C. Vicario, J. Manzi, I. Maurin, M. Coppey, J. Piehler, M. Dahan, *Adv. Mater.* **2017**, *29*, 17001809.
[20] I. P. Novoselova, A. Neusch, J.-S. Brand, M. Otten, M. R. Safari, N. Bartels, M. Karg, M. Farle, U. Wiedwald, C. Monzel, *Nanomaterials* **2021**, *11*, 2267.
[21] A. Neusch, U. Wiedwald, I. P. Novoselova, D. A. Kuckla, N. Tetos, S. Sadik, P. Hagemann, M. Farle, C. Monzel, *Nanoscale* **2024**, *16*, 15113.
[22] F. Sigmund, C. Massner, P. Erdmann, A. Stelzl, H. Rolbieski, M. Desai, S. Bricault, T. P. Wörner, J. Snijder, A. Geerlof, H. Fuchs, M. Hrabě de Angelis, A. J. R. Heck, A. Jasanoff, V. Ntziachristos, J. Plitzko, G. G. Westmeyer, *Nat. Commun.* **2018**, *9*, 1990.
[23] F. Sigmund, S. Pettinger, M. Kube, F. Schneider, M. Schifferer, S. Schneider, M. V. Efremova, J. Pujol-Martí, M. Aichler, A. Walch, T. Misgeld, H. Dietz, G. G. Westmeyer, *ACS Nano* **2019**, *13*, 8114.
[24] M. V. Efremova, S.-V. Bodea, F. Sigmund, A. Semkina, G. G. Westmeyer, M. A. Abakumov, *Pharmaceutics* **2021**, *13*, 397.

[25] T. Feggeler, J. Lill, D. Günzing, R. Meckenstock, D. Spoddig, M. V. Efremova, S. Wintz, M. Weigand, B. W. Zingsem, M. Farle, H. Wende, K. J. Ollefs, H. Ohldag, *New J. Phys.* **2023**, *25*, 043010.
[26] A. Pekarsky, O. Spadiut, *Front Bioeng Biotechnol* **2020**, *8*, 573183.
[27] T. J. Regan, H. Ohldag, C. Stamm, F. Nolting, J. Lüning, J. Stöhr, R. L. White, *Phys. Rev. B Condens. Matter* **2001**, *64*, 214422.
[28] C. Hartmann, M. Elsner, R. Niessner, N. P. Ivleva, *Appl. Spectrosc.* **2020**, *74*, 193.
[29] T. Mi, J. J. Wang, C. McCague, Y. Bai, *Cem. Concr. Compos.* **2023**, *143*, 105231.
[30] E. C. Sklute, S. Kashyap, M. D. Dyar, J. F. Holden, T. Tague, P. Wang, S. J. Jaret, *Phys. Chem. Miner.* **2018**, *45*, 1.
[31] F. M. Michel, V. Barrón, J. Torrent, M. P. Morales, C. J. Serna, J.-F. Boily, Q. Liu, A. Ambrosini, A. C. Cismasu, G. E. Brown Jr., *Proc. Natl. Acad. Sci. USA* **2010**, *107*, 2787.
[32] S. Miltenyi, W. Müller, W. Weichel, A. Radbruch, *Cytometry* **1990**, *11*, 231.
[33] C. Massner, F. Sigmund, S. Pettinger, M. Seeger, C. Hartmann, N. P. Ivleva, R. Niessner, H. Fuchs, M. H. de Angelis, A. Stelzl, N. L. Koonakampully, H. Rolbieski, U. Wiedwald, M. Spasova, W. Wurst, V. Ntziachristos, M. Winklhofer, G. G. Westmeyer, *Adv. Funct. Mater.* **2018**, *28*, 1706793.
[34] P. Müller, R. Gaebel, H. Lemcke, F. Wiekhorst, F. Hausburg, C. Lang, N. Zarniko, B. Westphal, G. Steinhoff, R. David, *Biomaterials* **2017**, *135*, 74.
[35] U. Wiedwald, M. Spasova, M. Farle, M. Hilgendorff, M. Giersig, *J. Vac. Sci. Technol. B Nanotechnol. Microelectron.* **2001**, *19*, 1773.
[36] M. Spasova, U. Wiedwald, R. Ramchal, M. Farle, M. Hilgendorff, M. Giersig, *J. Magn. Magn. Mater.* **2002**, *240*, 40.
[37] E. Myrovali, N. Maniotis, A. Makridis, A. Terzopoulou, V. Ntomprougkidis, K. Simeonidis, D. Sakellari, O. Kalogirou, T. Samaras, R. Salikhov, M. Spasova, M. Farle, U. Wiedwald, M. Angelakeris, *Sci. Rep.* **2016**, *6*, 37934.
[38] B. W. Zingsem, T. Feggeler, A. Terwey, S. Ghaisari, D. Spoddig, D. Faivre, R. Meckenstock, M. Farle, M. Winklhofer, *Nat. Commun.* **2019**, *10*, 4345.
[39] B. Zingsem, T. Feggeler, D. Spoddig, R. Meckenstock, M. Farle, M. Winklhofer, *Appl. Phys. Lett.* **2024**, *124*, 132405.
[40] M. V. Efremova, Y. A. Nalench, E. Myrovali, A. S. Garanina, I. S. Grebennikov, P. K. Gifer, M. A. Abakumov, M. Spasova, M. Angelakeris, A. G. Savchenko, M. Farle, N. L. Klyachko, A. G. Majouga, U. Wiedwald, *Beilstein J. Nanotechnol.* **2018**, *9*, 2684.
[41] Y. Zhang, X. Wang, C. Chu, Z. Zhou, B. Chen, X. Pang, G. Lin, H. Lin, Y. Guo, E. Ren, P. Lv, Y. Shi, Q. Zheng, X. Yan, X. Chen, G. Liu, *Nat. Commun.* **2020**, *11*, 5421.
[42] A. Van de Walle, A. Plan Sangnier, A. Abou-Hassan, A. Curcio, M. Hémadi, N. Menguy, Y. Lalatonne, N. Luciani, C. Wilhelm, *Proc. Natl. Acad. Sci. USA* **2019**, *116*, 4044.
[43] A. Fromain, A. Van de Walle, G. Curé, C. Péchoux, A. Serrano, Y. Lalatonne, A. Espinosa, C. Wilhelm, *Nanoscale* **2023**, *15*, 10097.
[44] T. W. Giessen, B. J. Orlando, A. A. Verdegaal, M. G. Chambers, J. Gardener, D. C. Bell, G. Birrane, M. Liao, P. A. Silver, *elife* **2019**, *8*, e46070.
[45] H. Aitken-Rogers, C. Singleton, A. Lewin, A. Taylor-Gee, G. R. Moore, N. E. Le Brun, *J. Biol. Inorg. Chem.* **2004**, *9*, 161.
[46] S. Mann, J. M. Williams, A. Treffry, P. M. Harrison, *J. Mol. Biol.* **1987**, *198*, 405.
[47] R. K. Watt, R. J. Hilton, D. M. Graff, *Biochim. Biophys. Acta* **2010**, *1800*, 745.
[48] A. J. Hudson, S. C. Andrews, C. Hawkins, J. M. Williams, M. Izuhara, F. C. Meldrum, S. Mann, P. M. Harrison, J. R. Guest, *Eur. J. Biochem.* **1993**, *218*, 985.
[49] V. J. Wade, A. Treffry, J. P. Laulhère, E. R. Bauminger, M. I. Cleton, S. Mann, J. F. Briat, P. M. Harrison, *Biochim. Biophys. Acta* **1993**, *1161*, 91.
[50] C. Cutler, A. Bravo, A. D. Ray, R. K. Watt, *J. Inorg. Biochem.* **2005**, *99*, 2270.
[51] J. S. Rohrer, Q. T. Islam, G. D. Watt, D. E. Sayers, E. C. Theil, *Biochemistry* **1990**, *29*, 259.
[52] N. D. Chasteen, P. M. Harrison, *J. Struct. Biol.* **1999**, *126*, 182.
[53] M. Koralewski, M. Pochylski, J. Gierszewski, *J. Nanopart. Res.* **2013**, *15*, 1902.
[54] D. Chambaere, E. De Grave, *J. Magn. Magn. Mater.* **1984**, *42*, 263.
[55] M. Testa-Anta, M. A. Ramos-Docampo, M. Comesaña-Hermo, B. Rivas-Murias, V. Salgueiriño, *Nanoscale Adv* **2019**, *1*, 2086.
[56] D. L. A. de Faria, F. N. Lopes, *Vib. Spectrosc.* **2007**, *45*, 117.
[57] I. Chamritski, G. Burns, *J. Phys. Chem. B* **2005**, *109*, 4965.
[58] C. P. Marshall, W. J. B. Dufresne, C. J. Rufledt, *J. Raman Spectrosc.* **2020**, *51*, 1522.
[59] I. V. Chernyshova, M. F. Hochella Jr., A. S. Madden, *Phys. Chem. Chem. Phys.* **2007**, *9*, 1736.
[60] M. Ibrahim Dar, S. A. Shivashankar, *RSC Adv.* **2014**, *4*, 4105.
[61] C. Liu, T. Stakenborg, S. Peeters, L. Lagae, *J. Appl. Phys.* **2009**, *105*, 102014.
[62] C. Wilhelm, C. Rivière, N. Biais, *Phys. Rev. E Stat. Nonlin. Soft Matter Phys.* **2007**, *75*, 041906.
[63] A. Neusch, U. Wiedwald, I. P. Novoselova, D. A. Kuckla, N. Tetos, S. Sadik, P. Hagemann, M. Farle, C. Monzel, *Nanoscale* **2024**, *16*, 15113.
[64] M. V. Dziuba, F.-D. Müller, M. Pósfai, D. Schüler, *Nat. Nanotechnol.* **2024**, *19*, 115.
[65] L. A. Maynard-Smith, L.-C. Chen, L. A. Banaszynski, A. G. L. Ooi, T. J. Wandless, *J. Biol. Chem.* **2007**, *282*, 24866.
[66] F. Wallberg, T. Tenev, P. Meier, *Cold Spring Harb. Protoc.* **2016**, *2016*, pdbprot087387.
[67] S. Kumar, M.-D. Filippi, *J. Vis. Exp.* **2016**.
[68] F. Pedregosa, G. Varoquaux, A. Gramfort, V. Michel, B. Thirion, O. Grisel, M. Blondel, G. Louppe, P. Prettenhofer, R. Weiss, R. J. Weiss, J. Vanderplas, A. Passos, D. Cournapeau, M. Brucher, M. Perrot, E. Duchesnay, *J. Mach. Learn. Res.* **2011**, *12*, 2825.
[69] T. Warwick, K. Franck, J. B. Kortright, G. Meigs, M. Moronne, S. Myneni, E. Rotenberg, S. Seal, W. F. Steele, H. Ade, A. Garcia, S. Cerasari, J. Denlinger, S. Hayakawa, A. P. Hitchcock, T. Tyliszczak, J. Kikuma, E. G. Rightor, H.-J. Shin, B. P. Tonner, *Rev. Sci. Instrum.* **1998**, *69*, 2964.
[70] P. Fischer, H. Ohldag, *Rep. Prog. Phys.* **2015**, *78*, 094501.
[71] J. Stöhr, *NEXAFS Spectroscopy*, Springer Science & Business Media, Berlin **2013**.
[72] T. Feggeler, A. Levitan, M. A. Marcus, H. Ohldag, D. A. Shapiro, *J. Electron Spectrosc. Relat. Phenom.* **2023**, *267*, 147381.
[73] R. J. Tuma, *Raman Spectrosc.* **2005**, *36*, 307.